February 1, 2011 | vol. 108 | no. 5 | pp. 1747–2172

PNAS

Proceedings of the National Academy of Sciences of the United States of America www.pnas.org


PNAS
Eyeball camera with
elastic arrays

Dynamically tunable hemispherical electronic eye camera system with adjustable zoom capability

Inhwa Jung[a], Jianliang Xiao[a], Viktor Malyarchuk[a], Chaofeng Lu[b,c], Ming Li[c,d], Zhuangjian Liu[e], Jongseung Yoon[a], Yonggang Huang[c,f,1], and John A. Rogers[a,1]

[a]Department of Materials Science and Engineering, Beckman Institute for Advanced Science and Technology, and Frederick Seitz Materials Research Laboratory, University of Illinois at Urbana-Champaign, Urbana, IL 61801; [b]Department of Civil Engineering, Zhejiang University, Hangzhou, Zhejiang 310058, China; [c]Department of Civil and Environmental Engineering, Northwestern University, Evanston, IL 60208; [d]State Key Laboratory of Structural Analysis for Industrial Equipment, Dalian University of Technology, Dalian 116024, China; [e]Institute of High Performance Computing, 1 Fusionopolis Way, #16-16 Connexis, Singapore 138632; and [f]Department of Mechanical Engineering, Northwestern University, Evanston, IL 60208

Edited by Eli Yablonovitch, University of California, Berkeley, CA, and approved December 10, 2010 (received for review October 14, 2010)

Imaging systems that exploit arrays of photodetectors in curvilinear layouts are attractive due to their ability to match the strongly nonplanar image surfaces (i.e., Petzval surfaces) that form with simple lenses, thereby creating new design options. Recent work has yielded significant progress in the realization of such "eyeball" cameras, including examples of fully functional silicon devices capable of collecting realistic images. Although these systems provide advantages compared to those with conventional, planar designs, their fixed detector curvature renders them incompatible with changes in the Petzval surface that accompany variable zoom achieved with simple lenses. This paper describes a class of digital imaging device that overcomes this limitation, through the use of photodetector arrays on thin elastomeric membranes, capable of reversible deformation into hemispherical shapes with radii of curvature that can be adjusted dynamically, via hydraulics. Combining this type of detector with a similarly tunable, fluidic plano-convex lens yields a hemispherical camera with variable zoom and excellent imaging characteristics. Systematic experimental and theoretical studies of the mechanics and optics reveal all underlying principles of operation. This type of technology could be useful for night-vision surveillance, endoscopic imaging, and other areas that require compact cameras with simple zoom optics and wide-angle fields of view.

biomimetic | electronic eyeball camera | flexible electronics | fluidic tunable lens | hydraulic actuation

Mammalian eyes provide the biological inspiration for hemispherical cameras, where Petzval-matched curvature in the photodetector array can dramatically simplify lens design without degrading the field of view, focal area, illumination uniformity, or image quality (1). Such systems use photodetectors in curvilinear layouts due to their ability to match the strongly nonplanar image surfaces (i.e., Petzval surfaces) that form with simple lenses (2–4). Historical interest in such systems has culminated recently with the development of realistic schemes for their fabrication, via strategies that overcome intrinsic limitations associated with the planar operation of existing semiconductor processes (4–6). The most promising procedures involve either direct printing of devices and components onto curved surfaces (6) or geometrical transformation of initially planar systems into desired shapes (1, 7–9). All demonstrated designs involve rigid, concave device substrates, to achieve improved performance compared to planar cameras when simple lenses with fixed magnification are used. Interestingly, biology and evolution do not provide guides for achieving the sort of large-range, adjustable zoom capabilities that are widely available in man-made cameras. The most relevant examples are in avian vision, where shallow pits in the retina lead to images with two fixed levels of zoom (50% high magnification in the center of the center of the field of view) (10). Also, changes in imaging properties occur, but in an irreversible fashion, during metamorphosis in amphibian vision to accommodate transitions from aquatic to terrestrial environments (11).

The challenge in hemispherical imagers is that, with simple optics, the curvature of the Petzval surface changes with magnification in a manner that leads to mismatches with the shape of detector array. This behavior strongly degrades the imaging performance, thereby eliminating any advantages associated with the hemispherical detector design. The solution to this problem demands that the curvature of the detector array changes in a coordinated manner with the magnification, to ensure identical shapes for the image and detector surfaces at all zoom settings. In the following, we report a system that accomplishes this outcome by use of an array of interconnected silicon photodetectors on a thin, elastomeric membrane, in configurations that build on advanced concepts of stretchable electronics (12–14). Actuating a fluidic chamber beneath the membrane causes it to expand or contract in a linear elastic, reversible fashion that provides precise control of the radius of curvature. Integrating a similarly actuated fluidic plano-convex lens yields a complete, hemispherical camera system with continuously adjustable zoom.

Results and Discussion

Fig. 1*A* provides a schematic illustration of the elements of the device and Fig. 1*B* shows a picture of an integrated system. The upper and lower components correspond to an adjustable, plano-convex zoom lens and a tunable, hemispherical detector array, respectively. The lens uses adapted versions of similar components described elsewhere (15–18); it consists of a water-filled cavity (1-mm thick, in the planar, unpressurized state) between a thin (0.2 mm) membrane of the transparent elastomer poly (dimethylsiloxane) (PDMS) on top and a glass window (1.5-mm thick) underneath. Pumping water into this cavity deforms the elastomer into a hemispherical shape, with a radius of curvature that depends on the pressure. This curvature, together with the index of refraction of the PDMS and water, defines the focal length of the lens and, therefore, the magnification that it can provide. Fig. 1*C* shows images of the detector array viewed through the fluidic lens, at two different positive pressures. The changes in magnification evident in Fig. 1*C* are reversible and can be quantified through measurement and mechanics modeling. Fig. 1*D* presents side view images and data collected at various states of deformation. The lens adopts an approximately hemispherical shape for all tuning states, with an apex height and radius of curvature (R_L) that change with pressure in a manner

Author contributions: I.J., J.X., V.M., Y.H., and J.A.R. designed research; I.J., J.X., V.M., C.L., M.L., Z.L., J.Y., Y.H., and J.A.R. performed research; I.J., J.X., V.M., C.L., M.L., Z.L., J.Y., Y.H., and J.A.R. contributed new reagents/analytic tools; I.J., J.X., V.M., C.L., M.L., Z.L., J.Y., Y.H., and J.A.R. analyzed data; and I.J., J.X., V.M., Y.H., and J.A.R. wrote the paper.

The authors declare no conflict of interest.

This article is a PNAS Direct Submission.

[1]To whom correspondence may be addressed. E-mail: jrogers@uiuc.edu or y-huang@northwestern.edu.

This article contains supporting information online at www.pnas.org/lookup/suppl/doi:10.1073/pnas.1015440108/-/DCSupplemental.

 www.pnas.org/cgi/doi/10.1073/pnas.1015440108

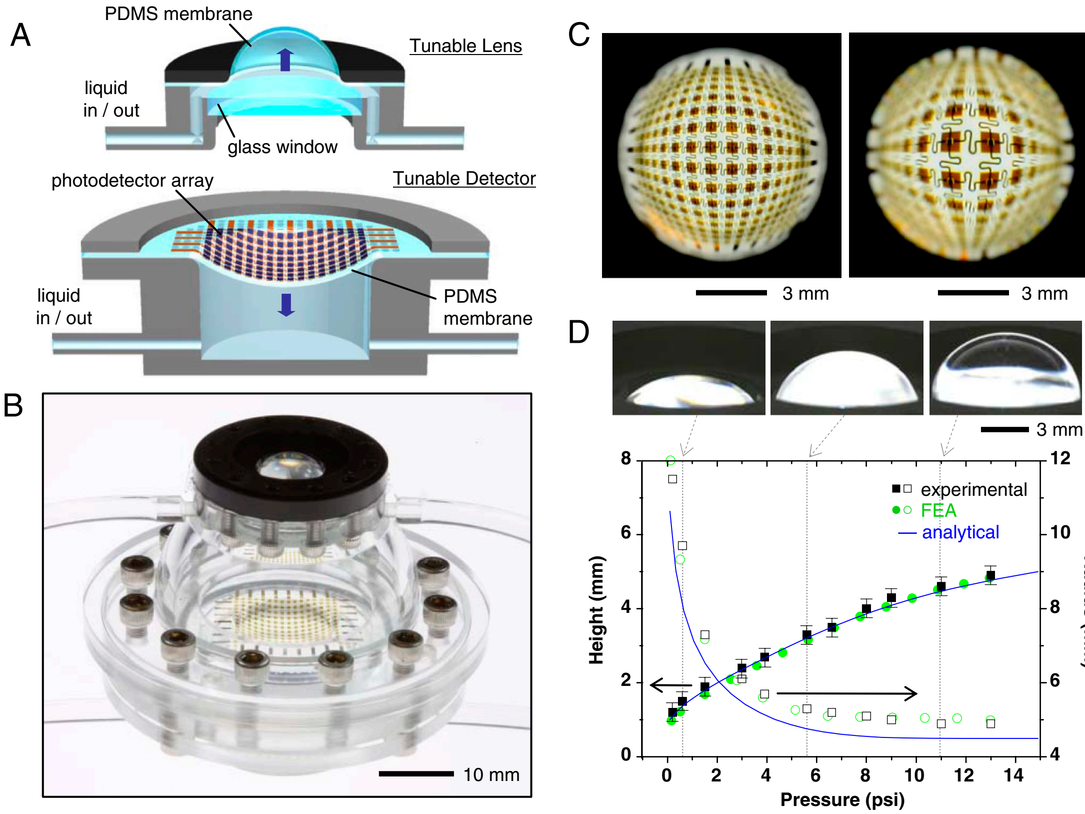

Fig. 1. (*A*) Schematic illustration of the camera, including the tunable lens (*Upper*) and tunable detector (*Lower*) modules. The lens consists of a fluid-filled gap between a thin (0.2 mm) PDMS membrane and a glass window (1.5-mm thick), to form a plano-convex lens with 9-mm diameter and radius of curvature that is adjustable with fluid pressure. The tunable detector consists of an array of interconnected silicon photodiodes and blocking diodes (16 × 16 pixels) mounted in a thin (0.4 mm) PDMS membrane, in a mechanically optimized, open mesh serpentine design. This detector sheet mounts on a fluid-filled cavity; controlling the pressure deforms the sheet into concave or convex hemispherical shapes with well-defined, tunable levels of curvature. (*B*) Photograph of a complete camera. (*C*) Photographs of the photodetector array imaged through the lens, tuned to different magnifications. The left and right images were acquired at radius of curvature in the lens of 5.2 and 7.3 mm. In both cases, the radius of curvature of the detector surface was 11.4 mm. The distance of the center part of the detector from the bottom part of the lens was 25.0 mm. (*D*) Angled view optical images of the tunable lens at three different configurations (*Upper*), achieved by increasing the fluid pressure from left to right. The lower frame shows measurements of the height and radius of curvature of the lens surface as a function of applied fluid pressure. The results reveal changes that are repeatable and systematic (experimental; □ and ■ symbols) and quantitatively consistent with analytical calculations of the mechanics (analytical; blue lines) and finite element analysis (FEA, green symbols).

quantitatively consistent with theory (blue curves) and finite element analysis (green circles), as shown in the graph of Fig. 1*D*. (Details on the lens profile appear in the *SI Appendix*.)

The most important, and most challenging, component of the camera is the tunable detector array. As is well known, the image formed by a plano-convex lens lies on a Petzval surface that takes the form of an elliptic paraboloid of revolution (1, 7), well approximated by a hemisphere in many cases of practical interest. The curvature depends strongly on magnification. As a result, the shape of the detector surface must change to accommodate different settings in the lens configuration. Fig. 1 *A* and *B* and Fig. 2 provide illustrations, images, and other details of a system that affords the required tunability, via stretchable designs actuated by hydraulics. The detector consists of an array of unit cells, each of which includes a thin (1.25 μm) silicon photodiode and blocking diode; the latter facilitates passive matrix readout. Narrow metal lines [Cr (5 nm)/Au (150 nm)] encapsulated with thin films of polyimide (~1 μm) on top and bottom provide ribbon-type interconnects between these cells, in a neutral mechanical plane layout that isolates the metal from bending induced strains. The interconnects have serpentine shapes to form an overall system with an open mesh geometry. These collective features enable the array to accommodate large strains associated with deformation of a thin (0.4 mm) supporting membrane of PDMS (13, 14). The fabrication involves planar processing of the devices and interconnects on a rigid substrate; release and transfer to the PDMS represents the final step. The area coverages of the device islands and the photosensitive regions are ~30% and ~13%, respectively. Previously reported mechanical designs can be used to achieve coverages up to ~60%.(9) Typical yields of working pixels were ~95%. An additional ~1–2% of the pixels fail after extensive mechanical cycling. For the images presented in the following, we used overscanning procedures to eliminate effects of defective pixels. (Details on device fabrication, transfer processes, hydraulic tuning systems, device yields, and overscanning procedures appear in *Materials and Methods* and the *SI Appendix*.)

Mounting the membrane with the photodector array bonded to its surface onto a plate with a circular opening (circular, with diameter *D*) above a cylindrical chamber (Fig. 1 *A* and *B*), filling this chamber with distilled water, and connecting input and output ports to an external pump prepares the system for pneumatic tuning. Fig. 2*A* shows tilted views of a representative device in its initial, flat configuration (i.e., no applied pressure; upper frame) and in a concave shape induced by extracting liquid out of the chamber (i.e., negative applied pressure; lower frame). (See Movie S1 for real-time operation of its deformation.) The exact shapes of the deformed surfaces, and the positions of the photodetectors in the array are both critically important to operation. A laser scanner tool (Next Engine) provided accurate measurements of the shapes at several states of deformation (i.e., applied pressures). For all investigated pressures, the detec-

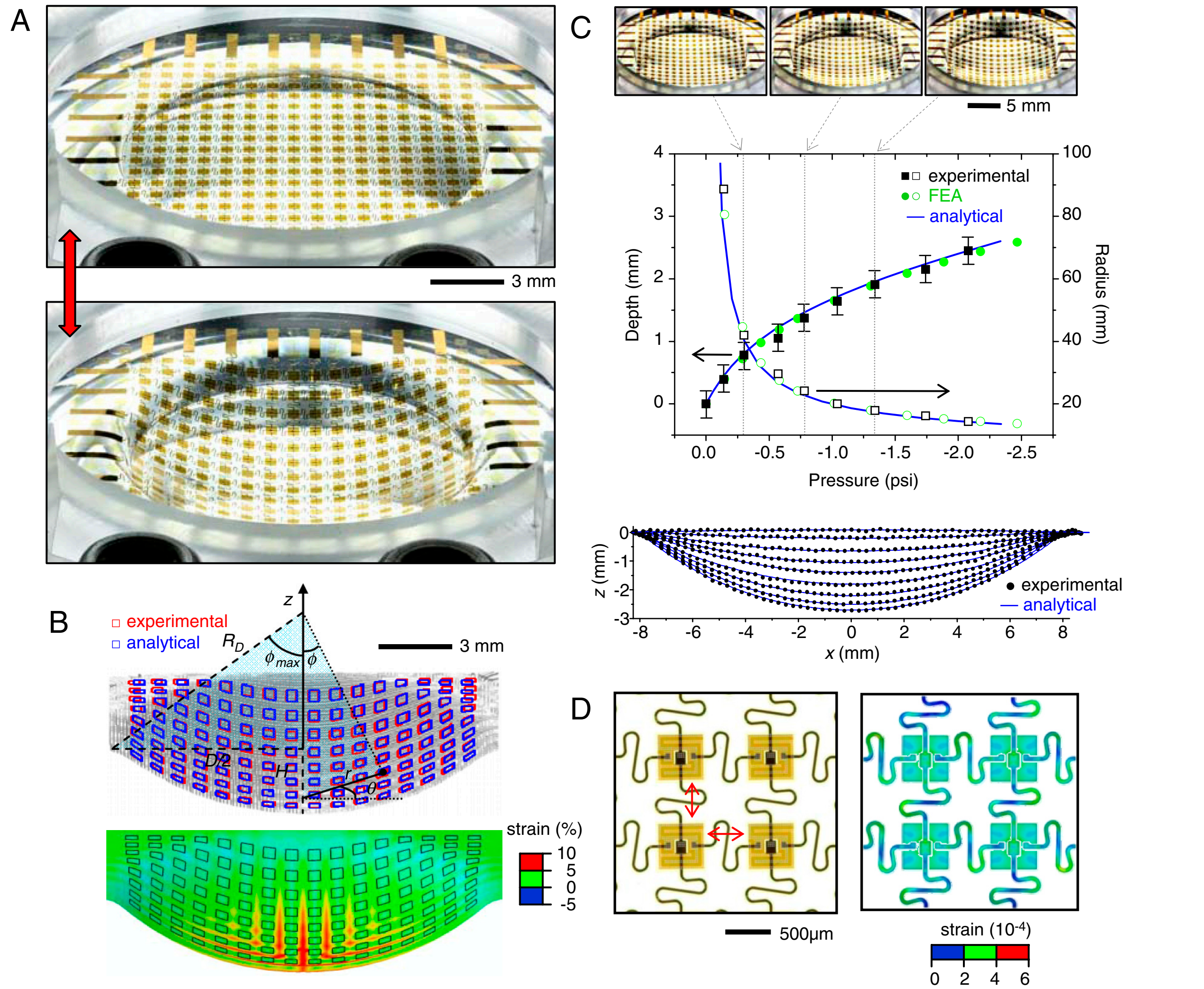

Fig. 2. (*A*) Tilted view of a photodetector array on a thin membrane of PDMS in flat (*Upper*) and hemispherically curved (*Lower*) configurations, actuated by pressure applied to a fluid-filled chamber underneath. (*B*) Three-dimensional rendering of the profile of the deformed surface measured by a laser scanner. Here, the shape is close to that of a hemisphere with a radius of curvature (R_D) of 13.3 mm and a maximum deflection (H_D) of 2.7 mm. Calculated (blue) and measured (red) unit cell positions appear as squares on this rendered surface. (*Upper*) Three-dimensional rendering of circumferential strains in the silicon devices (squares) and the PDMS membrane determined by finite element analysis (*Lower*). (*C*) Angled view optical images of the tunable detector in three different configurations (*Top*), achieved by decreasing the level of negative pressure applied to the underlying fluid chamber from left to right. Measurements of the apex height and radius of curvature of the detector surface as a function of applied fluid pressure reveal changes that are repeatable and systematic (experimental) and quantitatively consistent with analytical calculations of the mechanics (analytical; blue lines) and finite element analysis (FEA, green symbols), as shown in the middle frame. Laser scanning measurements of the profiles of the deformed detector surface show shapes are almost perfectly hemispherical, consistent with analytical mechanics models. Here, each measured profile (symbols) is accompanied by a corresponding analytical calculated result (lines) (*Bottom*). (*D*) Optical micrograph of a 2×2 array of unit cells, collected from a region near the center of a detector array, in a deformed state (*Left*) and maximum principal strains in the silicon and metal determined by finite element analysis (*Right*) for the case of overall biaxial strain of 12%. These strains are far below those expected to cause fracture in the materials.

tor surfaces exhibit concave curvature well characterized by hemispherical shapes. Fig. 2*B* shows a rendering of the laser-scanned surface. Measured profiles yield the peak deflection (H, at the center of the membrane) and the radius of curvature (R_D, also near the center). Top down images define the two-dimensional positions (i.e., along polar r and θ axes of Fig. 2*B*) of the photodetectors, at each deformed state. Projections onto corresponding measurements of the surface shape yield the heights (i.e., along the z axis). The outcomes appear as red squares in Fig. 2*B*. Comparison to analytical mechanics modeling of the positions (blue squares) shows excellent agreement. The photodetector surface deforms to a hemispherical shape due to water extraction, which implies a uniform meridional strain in the deformed surface, and therefore a uniform spacing between photodetectors in this direction (19). Mechanics analysis yields predictions for H as a function of the applied pneumatic pressure caused by water extraction and also a simple expression for the radius of curvature: $R_D = (D^2 + 4H^2)/(8H)$. Both results appear as blue curves in the middle frame of Fig. 2*C*; they show excellent agreement with experiment (black squares) and finite element analysis (green circles). A photodetector with an initial position given by $(r,\theta,0)$ in cylindrical coordinates on the flat surface moves to a new position given by $(R_D \sin\phi, \theta, R_D - H - R_D \cos\phi)$ on the deformed surface, where $\varphi = (2r/D)\sin^{-1}[4DH/(D^2 + 4H^2)]$ is the polar angle (*SI Appendix*, Fig. S1). (See *SI Appendix* for details on the modeling.) The analytically obtained photodetector positions are indicated as blue squares in the upper frame of Fig. 2*B*, which shows excellent agreement with both experiment and finite element analysis (lower frame of Fig. 2*B*), and therefore validates the hemispherical shape of the deformed detector surface. Similar modeling can be used to define the distribution of strains across both the PDMS membrane and the array of silicon photodiodes and blocking diodes. The results (Fig. 2*B*) show strains in both materials that are far below their thresholds for fracture (>150% for PDMS; ∼1% for silicon). The overall computed shape of the system also compares well to measurement. Further study illustrates that this level of agreement persists across all tuning states, as illustrated in Fig. 2*C*. Finite element analysis (lower frame of Fig. 2*B*) shows that the serpentine interconnects have negligible effects on the photodetector positions (20). Understanding their behavior is nevertheless important because they provide electrical interconnection necessary for operation. Three-dimensional finite element analysis of a square 2×2 cluster of four unit cells appears in Fig. 2*D*. The color shading shows the maximum principal strains in the silicon and metal, which are the most fragile materials in the detectors. The calculated peak strains in the materials are all exceptionally low, even for this case where the overall biaxial strain is ∼12%, corresponding to the point of highest strain in the array when tuned to the most highly curved configuration.

Fig. 3*A* presents a picture of a completed detector with external interconnection wiring to a ribbon cable that interfaces with an external data acquisition system (1). Here, a top-mounted fixture with a circular opening supports 32 electrode pins that mechanically press against corresponding pads at the periphery of the detector array. A compression element with four cantilever springs at each corner ensures uniformity in the applied pressure, to yield a simple and robust interconnection scheme (no failures for more than 100 tuning cycles). These features and the high yields on the photodetector arrays enable cameras that can collect realistic images, implemented here with resolution enhancements afforded by scanning procedures to allow detailed comparison to theory (see *SI Appendix*). To explore the basic operation, we first examine behavior with a fixed imaging lens. Representative images collected with the detector in planar and hemispherical configurations appear in Fig. 3*B*. The object in this case consists of a pattern of discs (diameters, 2 mm; distances between near neighbors, 3 mm; distances between distant neighbors, 5 mm), placed 75 mm in front of a glass plano-convex lens (diameter, 9 mm; focal length, 22.8 mm). The image in the flat state corresponds to a distance of 26.2 mm from the lens, or 5.5 mm closer to the lens than the nominal position of the image computed with thin lens equations. At this location, the regions of the image in the far periphery of the field of view (i.e., the four corners) are in focus. The center of the field of view is not simultaneously in focus because of the Petzval surface curvature associated with the image. Deforming the detector array into a concave shape moves the center region away from the lens and toward the position of the image predicted by the thin lens equation. The hemispherical shape simultaneously aligns other parts of the detector with corresponding parts of the image. As a result, the entire field of view comes into focus at once. Planar projections of these images are shown in Fig. 3*C*. Simulated images based on experimental parameters appear in Fig. 3*D*. The results used ray-tracing calculations and exploited the cylindrical symmetry of the device (21, 22). In particular, fans

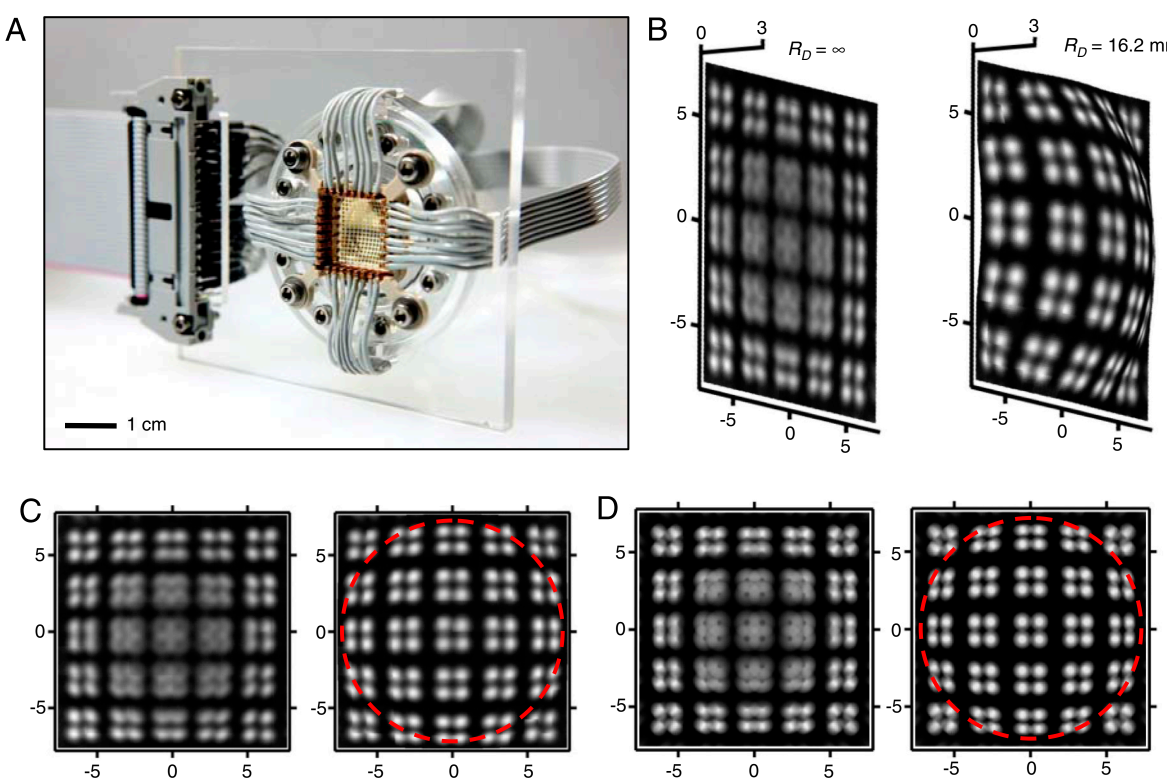

Fig. 3. (*A*) Photograph of a deformable detector array with external electrical interconnections. Electrode pins on a mounting plate press against matching electrodes at the periphery of the array to establish connections to a ribbon cable that leads to a data acquisition system. (*B*) Images of a test pattern of bright circular discs, acquired by the device in flat (*Left*) and deformed hemispherical (*Right*) configurations, collected using a glass plano-convex lens (diameter, 9 mm; focal length, 22.8 mm). The images are rendered on surfaces that match those of the detector array. The distance between the lens and the source image is 75 mm. The radius of curvature and the maximum deflection in this deformed state are 16.2 and 2.2 mm, respectively. The image in the flat case was collected at a distance of 5.5 mm closer to the lens than the focal location expected by the thin lens approximation (31.7 mm). In this position, only the far peripheral regions of the image are in focus. The image in the curved configuration was acquired simply by actuating the detector into this shape, without changing any other aspect of the setup. This deformation brings the entire field of view into focus, due to matching of the detector shape to the Petzval surface. (*C*) Planar projections of these images. The dashed circle indicates the area under deformation. (*D*) Modeling results corresponding to these two cases, obtained by ray-tracing calculation. The outcomes show quantitative agreement with the measurements. The dashed circle indicates the area under deformation.

of rays originating at the object (75 mm in front of the lens) were propagated through the system to determine relevant point spread functions (PSFs). Placing corresponding PSFs for every point at the object plane, using a total of 10,000 rays, onto the surface of a screen defined by the shape of the detector yielded images suitable for direct comparison to experiment.

To demonstrate full capabilities and adjustable zoom, we acquired images with the tunable, fluidic lens. Ray-tracing analysis for the case of an object at 67 mm from the lens provided matched parameters of R_L, R_D, and z, the distance to the center of the image surface, as example configurations for different magnification settings. Fig. 4*A* shows two-dimensional representations of Petzval surfaces for four different lens shapes, all plano-convex with hemispherical curvature, corresponding to (R_L, R_D, z) values of (4.9, 11.4, 16 mm), (6.1, 14.0, 24 mm), (7.3, 19.2, 38 mm), and (11.5, 25.7, 55 mm). As expected, increasing R_L increases the focal length and the magnification, thereby increasing z and R_D. Current setups involve manual adjustment of the

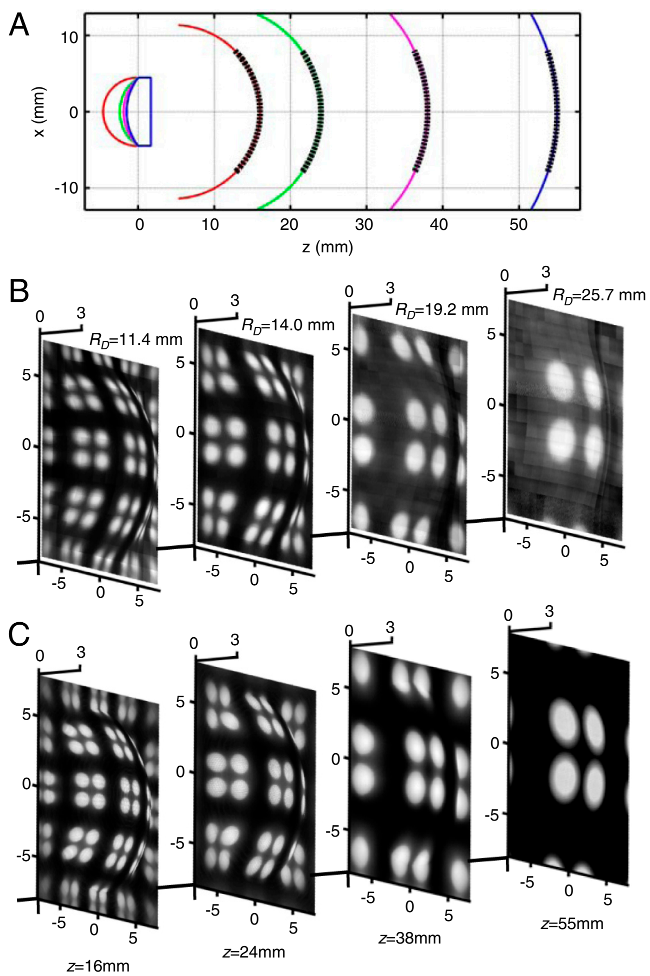

Fig. 4. (*A*) Ray-tracing analysis of the positions and curvatures of the image surfaces (i.e., Petzval surfaces; *Right*) that form with four different geometries of a tunable plano-convex lens (*Left*). Actual sizes of detector surfaces are shown as dashed lines. (*B*) Images acquired by a complete camera system, at these four conditions. These images were collected at distances from the lens (z) of 16, 24, 38, and 55 mm with corresponding radii of curvature of the lens surface (R_L) of 4.9, 6.1, 7.3, and 11.5 mm. The radii of curvature (R_D) of the detector surface, set to match the computed Petzval surface shape, were 11.4, 14.0, 19.2, and 25.7 mm. These images were acquired by a scanning procedure described in *Materials and Methods* The object consists of a pattern of light circular discs (diameter, 3.5 mm; pitches between circles, 5 and 8.5 mm). (*C*) Images computed by ray-tracing analysis, at conditions corresponding to the measured results. The axis scales are in millimeters.

distance between the detector and the lens. Images collected at these four settings appear in Fig. 4*B*. The object in this case is an array of circular discs, similar to those used in Fig. 3, but with diameters of 3.5 mm, pitch values of 5 and 8.5 mm. The optical magnifications are 0.24, 0.36, 0.57, and 0.83, corresponding to a 3.5× adjustable zoom capability. Uniformity in focus obtains for all configurations. (Further comparison with flat detector appears in the *SI Appendix*.) Optical modeling, using the same techniques for the results of Fig. 3, show quantitative agreement.

Conclusions

The results demonstrate that camera systems with tunable hemispherical detector arrays can provide adjustable zoom with wide-angle field of view, low aberrations, using only a simple, single-component, tunable plano-convex lens. The key to this outcome is an ability to match the detector geometry to a variable Petzval surface. This type of design could complement traditional approaches, particularly for applications where compound lens systems necessary for planar or fixed detectors add unwanted size, weight, or cost to the overall system; night-vision cameras and endoscopes represent examples. Although the fill factor and total pixel count in the reported designs are moderate, there is nothing fundamental about the process that prevents significant improvements. The hydraulic control strategy represents one of several possible actuation mechanisms. Although the present design incorporates two separate pumps and manual z-axis positioning, with suitable setups it should be possible for a single actuator to adjust both lens and detector, and their separation, simultaneously, in a coordinated fashion. These kinds of concepts, or other approaches in which microactuators are embedded directly on the elastomer, as a class of hybrid hard and soft microelectromechanical system device, might be useful to explore.

Materials and Methods

Fabrication of Silicon Photodetector Arrays on Elastomeric Membranes. The detector arrays were made by doping a sheet of silicon in a configuration designed for pairs of photodiodes and blocking diodes in a 16 × 16 square matrix. In particular, the top layer of an silicon on insulator wafer (1.25-μm-thick silicon on a 400-nm-thick layer of silicon dioxide on a silicon substrate, *p* type, ⟨100⟩ direction, Soitec) was *p* and *n* doped sequentially through a masking layer of silicon dioxide (900-nm thick) deposited by plasma-enhanced chemical vapor deposition (SLR730, Unaxis/Plasma-Therm) and patterned by photolithography and etching. For *p* doping, the sample was exposed to a boron source for 30 min at 1,000 °C in an N_2 environment (custom 6-in. tube furnace). The *n* doping used a phosphorous source under the same conditions for 10 min (Model 8500 Dual-Stack Diffusion/Oxidation Furnaces, Lindberg/Tempress). Each unit cell was then isolated by reactive ion etching (RIE; Unaxis/Plasma-Therm) through the silicon layer in a patterned defined by photolithography. Interconnects consisted of metal lines [Cr (5 nm)/Au (150 nm)] deposited by sputtering (AJA International, Inc.) and encapsulated with polyimide (~1 μm, from polyamic acid solution, Sigma Aldrich) on top and bottom. Just prior to transfer, the buried silicon dioxide was removed by wet etching (30 min, hydrofluoric acid 49%) through an array of holes (3 μm in diameter) etched through the silicon.

A stamp of PDMS (SYLGARD 184 Silicone elastomer kit, Dow Corning) was used to transfer the resulting photodetector array to a thin (0.4 mm) membrane of PDMS that was preexposed to ultraviolet-induced ozone for 2.5 min. Before peeling back the stamp, the entire assembly was baked at 70 °C for 10 min to increase the strength of bonding between the array and the membrane.

Completing the Tunable Detector System. The membrane supporting the detector array was cut into a circular shape (49 mm in diameter), and then placed on a machined plate with a hole (13 or 15 mm in diameter) at the center. A cylindrical chamber, with volume of 3.5 mL, was then attached to the bottom of this plate. The membrane was mechanically squeezed at the edges to form a seal and, at the same time, to yield slight radial tensioning, through the action of structures on the plate designed for this purpose. The bottom chamber has two inlets, one of which connects to a stop cock (Luer-lock polycarbonate stop cocks, McMaster-Carr) and the other to a custom syringe pump capable of controlling the volume of liquid moving in and out of the camber with a precision of ~0.05 mL. Distilled water fills the system. A gauge (diaphragm gauge 0 ~ 3 psi, Noshok) was used to monitor the pressure.

For electrical connection, the top insulating layers covering the electrode pads at the periphery of the detector array were removed by RIE (CS 1701 Reactive Ion Etching System, Nordson MARCH) through an elastomeric shadow mask. These electrodes press against copper electrode pins on a mounting plate designed with four cantilever springs at its corners. To ensure good electrical contact, the surfaces of the pins were polished and then coated with metal layers by electron beam deposition [Cr (20 nm)/Au (400 nm)]. Each electrode pin was connected to an electrical wire using conductive epoxy (CW2400, Chemtronics); these wires were assembled with a pin connector which connects to a ribbon cable.

Fabricating the Tunable Lens. The tunable lens simply consists of a thin PDMS membrane (0.2 mm in thickness, 25.4 mm in diameter) and a glass window (12.5 mm in diameter, 1.5 mm in thickness; Edmund Optics) attached to a plastic supporting piece by epoxy (ITW Devcon). The separation between the PDMS membrane and the glass window was ~1 mm. To ensure a water-tight seal, the membrane was squeezed between two plastic plates. A hole in the top plate defined the diameter of the lens (9 mm). Gauges (diaphragm gauge 0 ~ 10 psi, Noshok; differential gauge 0 ~ 20 psi, Orange Research) were used to measure the pressure.

Capturing Images. Diffusive light from an array of light emitting diodes (MB-BL4X4, Metaphase Technologies) provided a source for illumination. The objects consisted of printed transparency films (laser photoplotting, CAD/Art Services) or metal plates machined by laser cutting. In all cases, images were rendered by combining datasets collected by stepping the detector along two orthogonal axes x, y normal to the optic axis. Either 10 or 20 steps with spacings of 92 μm for each axis were used to achieve effective resolutions of 100 times larger than the number of photodetectors. Lookup tables and automated computer codes were used, in some cases, to eliminate the effects of malfunctioning pixels.

ACKNOWLEDGMENTS. We thank T. Banks, and J.A.N.T. Soares for help using facilities at the Frederick Seitz Materials Research Laboratory. The authors also appreciate M.J. Kim, D. Stevenson, G. Shin, K.J. Yu, J.H. Lee, D.H. Kim, D.G. Kim, H.C. Ko, and J.S. Ha for valuable comments and help. The fundamental aspects of hard and soft materials integration and the overall system construction were supported by Defense Advanced Research Planning Agency N66001-10-1-4008 and Sharp. The optical design and the theoretical mechanics were supported by National Science Foundation Emerging Frontiers in Research and Innovation, and Electrical, Communications, and Cyber Systems ECCS-0824129, respectively.

1. Ko HC, et al. (2008) A hemispherical electronic eye camera based on compressible silicon optoelectronics. *Nature* 454:748–753.
2. Grayson T (2002) Curved focal plane wide field of view telescope design. *Proc SPIE* 4849:269–274.
3. Rim SB, et al. (2008) The optical advantages of curved focal plane arrays. *Opt Express* 16:4965–4971.
4. Dinyari R, et al. (2008) Curving monolithic silicon for nonplanar focal plane array applications. *Appl Phys Lett* 92:091114-1–091114-3.
5. Hung PJ, Jeong KH, Liu GL, Lee LP (2004) Microfabricated suspensions for electrical connections on the tunable elastomer membrane. *Appl Phys Lett* 85:6051–6053.
6. Xu X, Davanco M, Qi XF, Forrest SR (2008) Direct transfer patterning on three dimensionally deformed surfaces at micrometer resolutions and its application to hemispherical focal plane detector arrays. *Org Electron* 9:1122–1127.
7. Jung I, et al. (2010) Paraboloid electronic eye cameras using deformable arrays of photodetectors in hexagonal mesh layouts. *Appl Phys Lett* 96:021110-1–021110-3.
8. Ko HC, et al. (2009) Curvilinear electronics formed using silicon membrane circuits and elastomeric transfer elements. *Small* 5:2703–2709.
9. Shin G, et al. (2010) Micromechanics and advanced designs for curved photodetector arrays in hemispherical electronic-eye cameras. *Small* 6:851–856.
10. Proctor NS, Lynch PJ (1993) *Manual of Ornithology: Avian Structure and Function* (Yale Univ Press, New Haven, CT).
11. Hoskins SG (1990) Metamorphosis of the amphibian eye. *J Neurobiol* 21:970–989.
12. Khang DY, Jiang HQ, Huang Y, Rogers JA (2006) A stretchable form of single-crystal silicon for high-performance electronics on rubber substrates. *Science* 311:208–212.
13. Kim DH, et al. (2009) Ultrathin silicon circuits with strain-isolation layers and mesh layouts for high-performance electronics on fabric, vinyl, leather, and paper. *Adv Mater* 21:3703–3707.
14. Kim DH, et al. (2008) Materials and noncoplanar mesh designs for integrated circuits with linear elastic responses to extreme mechanical deformations. *Proc Natl Acad Sci USA* 105:18675–18680.
15. Tsai FS, et al. (2008) Miniaturized universal imaging device using fluidic lens. *Opt Lett* 33:291–293.
16. Tsai FS, et al. (2010) Fluidic lens laparoscopic zoom camera for minimally invasive surgery. *J Biomed Opt* 15:030504-1–030504-3.
17. Yu HB, Zhou GY, Leung HM, Chau FS (2010) Tunable liquid-filled lens integrated with aspherical surface for spherical aberration compensation. *Opt Express* 18:9945–9954.
18. Zhang DY, et al. (2003) Fluidic adaptive lens with high focal length tunability. *Appl Phys Lett* 82:3171–3172.
19. Wang SD, et al. (2009) Mechanics of hemispherical electronics. *Appl Phys Lett* 95:181912-1–181912-3.
20. Song J, et al. (2009) Mechanics of noncoplanar mesh design for stretchable electronic circuits. *J Appl Phys* 105:123516-1–123516-6.
21. Born M, Wolf E (1999) *Principles of Optics* (Cambridge Univ Press, New York), pp 204–210.
22. Walther A (1995) *The Ray and Wave Theory of Lenses* (Cambridge Univ Press, Cambridge, UK), pp 283–294.

Supporting Information

Jung et al. 10.1073/pnas.1015440108

Table of Contents

Supplementary Methods and Discussion

The following provides information on fabricating and transferring the photodetector array, on the pneumatic tuning system and electrical connection hardware, on techniques for determining the surface geometry and pixel positions, on the mechanical analysis and on evaluation of the tunable lens and the imaging process.

Fabrication Process of Photodetector Array and I-V Characteristics

The steps for fabricating the photodetector array generally follow procedures previously reported(1), although the specific designs here are adapted for to allow tunable mechanics and improved performance in the photodetectors. For the latter, the major changes are in the use of the solid source doping, both for *p* and *n* type, to replace the use of spin-on-dopants. The response of a representative individual pixel appears in the Fig. S1. Detailed fabrication procedures are as follows.

Fabrication procedure for photodetector array

p+ doping

1. Clean 1.25μm SOI wafer (acetone, IPA, water, drying at 110°C for 5min).
2. Clean by HF for 2s.
3. Deposit PECVD SiO_2 900nm.
4. Treat with HMDS for 1.5min.
5. Pattern PR (p+ doping).
6. Anneal at 110°C for 5min.
7. Etch oxide in BOE for 2.5min.
8. Remove PR by acetone and clean by piranha for 3min.
9. Expose to diffusive boron source at 1000°C for 30min.
10. Clean the processed wafer (HF 1min, piranha 10min, BOE 1min).

n+ doping

11. Deposit PECVD SiO_2 900nm.
12. Treat with HMDS for 1.5min.
13. Pattern PR (n+ doping).
14. Anneal at 110°C for 5min.
15. Etch oxide in BOE for 2.5min.

16. Remove PR by acetone and clean by piranha for 3min.

17. Expose to diffusive phosphorus source at 1000°C for 10min.

18. Clean the processed wafer (HF 1min, piranha 10min, BOE 1min).

Silicon isolation

19. Pattern PR (Si isolation).

20. Etch silicon by RIE (50mTorr, 40sccm SF_6, 100W, 3min).

21. Remove PR by acetone and clean by piranha for 3min.

Sacrificial oxide layer deposition

22. Etch oxide layer of SOI wafer in HF for 1.5min.

23. Deposit PECVD SiO_2 100nm.

24. Treat with HMDS for 1.5min.

25. Pattern PR (sacrificial layer).

26. Anneal at 110°C for 5min.

27. Etch PECVD oxide in BOE for 30s.

28. Remove PR by acetone and clean by piranha for 3min.

Deposit 1st PI

29. Spin coat with PI (4000rpm, 60s).

30. Anneal at 110°C for 3min at 150°C for 10min.

31. Anneal at 250°C for 2h in N_2 atmosphere.

Pattern via holes

32. Expose to ultraviolet induced ozone (UVO) for 5min.

33. Deposit PECVD SiO_2 150nm.

34. Treat with HMDS for 1.5min.

35. Pattern PR (via pattern).

36. Etch PECVD oxide by RIE (50mTorr, 40:1.2sccm CF_4:O_2, 150W, 8.5min).

37. Remove PR by acetone.

38. Etch PI by RIE (150mTorr, 20sccm O_2, 150W, 20min).

Metallization

39. Etch PECVD oxide in BOE for 35s.

40. Sputter 5/150nm of Cr/Au by sputter coater (AJA international).

41. Pattern PR (metal pattern).

42. Anneal at 110°C for 5min.

43. Etch Au/Cr by wet etchants for 40/20s.

44. Remove PR by acetone (carefully).

Deposit 2nd PI

45. Spin coat with PI (4000rpm, 60s).
46. Anneal at 110°C for 3min at 150°C for 10min.
47. Anneal at 250°C for 2h in N_2 atmosphere.

Pattern etch holes

48. Expose to ultraviolet induced ozone (UVO) for 5min.
49. Deposit PECVD SiO_2 150nm.
50. Treat with HMDS for 1.5min.
51. Pattern PR (hole pattern).
52. Etch PECVD oxide by RIE (50mTorr, 40:1.2sccm CF_4:O_2, 150W, 8.5min).
53. Remove PR by acetone.
54. Etch PI by RIE (150mTorr, 20sccm O_2, 150W, 12min).
55. Etch Au/Cr by wet etchants for 20/5s.
56. Etch PI by RIE (150mTorr, 20sccm O_2, 150W, 15min).
57. Etch silicon by RIE (50mTorr, 40sccm SF_6, 100W, 3min).

PI isolation

58. Etch PECVD oxide in BOE for 35s.
59. Expose to ultraviolet induced ozone (UVO) for 5min.
60. Deposit PECVD SiO_2 150nm.
61. Treat with HMDS for 1.5min.
62. Pattern PR (PI isolation).
63. Etch PECVD oxide by RIE (50mTorr, 40:1.2sccm CF_4:O_2, 150W, 8.5min).
64. Remove PR by acetone.
65. Etch PI by RIE (150mTorr, 20sccm O_2, 150W, 40min).

Method for Transferring Device Array and Completing Camera

In general, the transfer procedure followed methods reported previously (2). Fig. S2 illustrates each step. For transfer, we manually controlled the speed of releasing the flat PDMS stamp at each stage. The device array is first lifted onto a flat PDMS stamp, by fast retraction from the fabricated silicon source substrate. (~0.1sec) Then, the device array is transferred to a thin PDMS membrane. In this case, the flat PDMS stamp is slowly removed (~10sec). The transfer process is mostly successful owing to higher bonding force between silicon surface (device bottom) and PDMS than the force between polyimide (device top) and PDMS. (3) To ensure perfect transfer, the target PDMS substrate is treated with ultraviolet induced ozone and baked at 70°C. Detailed procedures are as follows.

Transfer scheme for silicon photodetector array

1. Etch oxide layer of SOI wafer in HF for 30min.
2. Rinse the processed wafer with DI water for 10min (carefully).
3. Clean device perimeter using scotch tapes.
4. Pick up photodetector array using a flat PDMS (Sylgard 184, Dow Corning) stamp.
5. Expose ultraviolet induced ozone (UVO) to a target substrate (thin PDMS) for 2.5min.
6. Stamp to a target substrate (don't release PDMS stamp).
7. Post-bake at 70°C for 10min.
8. Release PDMS stamp (slowly ~ 10sec).

Method for Tuning the Lens and the Detector Surface Geometry

Fig. S3*A* shows a fabricated silicon-based photodetector array before transfer and Fig. S3*B* shows the transferred device array on a circular PDMS membrane. This PDMS membrane served as a substrate and also as a component for sealing the pneumatic tuning system. This system consists of several components, shown in Fig. S4*A*. To ensure perfect sealing, the PDMS membrane is squeezed by the upper and the lower covers. Although the system is effectively sealed by this design, the membrane is significantly deformed by compression. As a result, additional components were designed to stretch the deformed membrane, to ensure a flat surface. This element resulted in 2~3% of pre-strain (ε_0). The opening hole element is used to control the size and shape of deformation. Fig. S4*B* shows the assembled device array with the pneumatic tuning system. This assembly is connected with the fluidic chamber (the lowest part in Fig. S4*A*). This fluidic chamber has two liquid input/output ports. As in Fig. S5*A*, these ports are connected to plastic tubing and to either a stop cock or a custom made syringe. These ports are used not only for applying pressure but also for releasing air/bubble entrapped in the system. The stop-cock is closed after air/bubble is released. For tunable fluidic lens, we used a liquid-core solid-cladding lens geometry(4-7) due its simplicity over liquid-core liquid-cladding designs(8-11). Fig. S5*C*, *D* show the tunable lens. As in this case with the tunable detector, the tunable lens also incorporates a deformable PDMS membrane. This membrane is squeezed to ensure sealing. In this case, a pre-straining element is not included in the design, partly because the the membrane surface is deformed in its initial state. To measure the pressure inside of the tunable lens and the tunable detector system, a pressure gauge is connected through a *t*-connector. Several pressure gauges are used depending on range of pressure inside of systems. (diaphragm gauges 0 ~ 3 psi, 0 ~ 10 psi, Noshok, differential gauge 0 ~ 20 psi, Orange Research). Detailed step-by step procedures for completing the tunable detector system are as follows.

Procedures for completing the tunable detector

1. Open electrodes covering with PDMS by RIE (150mTorr, 20sccm O_2, 150W, 1h).
2. Cut PDMS membrane with device through a cutting pad.
3. Install PDMS membrane to the fluidic deformation system.
4. Assemble and align the metal electrodes pin array and install onto the plastic board.
5. Assemble fluidic chamber and connect in/outlet tubes with a stop cock.
6. Insert distilled water into the system using a syringe.
7. Remove bubbles from the system and close the stop cock.

Method for Establishing Electrical Connection and Device Yield

Establishing electrical connection between the device array and the external data acquisition system was a significant challenge for completing a working camera. In previous, static hemispherical camera designs, metal layers deposited through elastomeric shadow masks(1) or patterns of silver epoxy connected electrodes of the device array to those on a printed computer board(12, 13). However, these methods could not be applied to the tunable system due to significant deformation of PDMS substrate, particularly due to stress concentrations at the edges. A special fixture system which can make electrical contact with device on a flexible substrate by mechanical pressing was designed. Fig. S6*A* shows bottom-up view of the hardware which consists of 32 copper pin electrodes. These pins are designed to press against electrodes of device array using cantilever springs. (Fig. S6*B*, *E*) To reduce the contact resistance, the surfaces of electrode pins are polished and coated with metal layers (Cr/Au, 20nm/400nm). Fig. S6*C*, *D* show these 32 pins aligned and in contact with device electrodes. The inset shows more clearly that these electrode pins press against electrodes of device array. This hardware also stretches the membrane slighting to form a perfect flat surface. Fig. S6*E* shows that electrical wires are attached to electrode pins for further interface with the LABVIEW data acquisition system (1). This electrical connection hardware made successful electrical contact over entire 32 electrodes. Fig. S7 shows a test imaging result from the tunable detector imaging system using this electrical contact hardware. The result reveals that electrical contact is successfully made over all electrodes. (100% contact yields) However, it is observed that 11 pixels out of 256 pixels (95% pixel yields) are not working properly. In these cases, overscanning was used to eliminate the effects of defective pixel elements.

Determination of the Lens and the Detector Surface Geometry

At several states of deformation, three dimensional geometries of the deformed surfaces were determined by 3D laser scanner. (Next Engine, The Imaging Technology Group, Beckman Institute for Advanced Science and Technology, University of Illinois at Urbana-Champaign) Fig. S8*A* shows this 3D laser scanning tool configured for measuring geometry of detector surface. Fig. S8*B*, *C* are close-up views of the tunable detector and the tunable lens which are being scanned. Fig. S9*A* shows three dimensional rendering of raw data of a deformed surface of the tunable lens. To determine the radius of curvature and the apex height of deformed surface, a MATLAB code is used. Fig. S9*B* shows the center profile at several states of deformations. Although the lens profile around the apex fitted well with a circle, the total profile not perfectly matched with a circle. This is due to the deformation of PDMS membrane after initial installation, induced by squeezing. As a result, the radius of curvature is determined differently depending on the range of data for fitting. (Fig. S9*B*, *C*) However, the radius of curvature fitted from a partial range is used as the parameter of the lens, because the calculated focal distance agreed with the real measurement when this value is used as a parameter for ray-tracing calculation.

The geometry of detector surface can be determined similarly. Fig. S10*A* shows raw data from the deformed detector surface. Whereas lens surfaces can be fitted to a circle around the apex, detector surfaces are fitted with a circle over entire deformed surface. (See Fig. 2*C* in the main text.) This is due to the pre-straining element which is designed to stretch the PDMS membrane after installation. (See Fig. S4*A*.) To determine the pixel position, a top-down view of device array obtained at the same deformation state is used. From this picture, *x, y* pixel positions are determined using AutoCad. Then, the height information is obtained by projecting onto the deformed surface (Fig. S10*B*). Fig. S10*D* shows determined pixel positions overdrawn on the projected top-down view. Determined positions also match with the analytically calculated positions. (Fig. S10*E*)

Mechanics of the Tunable Lens

The PDMS membrane of thickness t=0.2 mm in the tunable lens is confined by an open hole (of diameter D=9 mm) on a water chamber. Water injection into the chamber induces a pressure difference p between the two surfaces of PDMS, which deforms the PDMS membrane to a large strain (>40%). Since PDMS is nearly incompressible and displays nonlinear material behavior under large strain (14), it can be represented by the Yeoh hyperelastic material model with the elastic energy density function given by (15)

$$U = \sum_{n=1}^{3} C_n \left(I_1 - 3\right)^n , \qquad [\mathbf{1}]$$

where C_n are material constants, $I_1 = \lambda_1^2 + \lambda_2^2 + \lambda_3^2$ is the first invariant of the left Cauchy-Green deformation tensor, and λ_i are the principal stretches which satisfy $\lambda_1\lambda_2\lambda_3 = 1$ due to incompressibility.

For uniaxial tension, $\lambda_1 = 1 + \varepsilon = \lambda$, which gives $\lambda_2 = \lambda_3 = 1/\sqrt{\lambda}$, $I_1 = \lambda^2 + 2/\lambda$, and stress

$$\sigma = 2\left(\lambda^2 - \frac{1}{\lambda}\right)\left[C_1 + 2C_2\left(I_1 - 3\right) + 3C_3\left(I_1 - 3\right)^2\right]. \qquad [\mathbf{2}]$$

For PDMS (sylgard 184), the uniaxial tensile stress-strain data (14) give

$$C_1 = 0.285 MPa , \quad C_2 = 0.015 MPa , \quad C_3 = 0.019 MPa . \qquad [\mathbf{3}]$$

The shape of the lens after water injection depends on its deflection.

(1) For $H \le D/2$, the lens deforms to a spherical cap, as shown in Fig. S11*A*. The spherical radius and polar angle are

$$R = \frac{D^2 + 4H^2}{8H}, \quad \varphi_{\max} = \sin^{-1}\frac{D}{2R} \qquad [\mathbf{4}]$$

For a point initially at $(r, \theta, 0)$ in cylindrical coordinates, its polar angle on the deformed surface is $\varphi = \frac{2r}{D}\varphi_{\max}$. The principle stretches are

$$\lambda_1 = \frac{2R\varphi_{\max}}{D}, \quad \lambda_2 = \frac{R\sin\varphi}{r}, \quad \lambda_3 = \frac{1}{\lambda_1\lambda_2} = \frac{Dr}{2R^2\varphi_{\max}\sin\varphi}. \qquad [\mathbf{5}]$$

The elastic strain energy is obtained as

$$U_{\mathrm{e}} = 2\pi t \int_0^{D/2} \sum_{n=1}^{3} C_n \left(I_1 - 3\right)^n r\mathrm{d}r . \qquad [\mathbf{6}]$$

The work done by the pressure is

$$W = pV = \frac{\pi}{3} pH^2\left(3R - H\right), \qquad [\mathbf{7}]$$

where $V = \pi H^2\left(3R - H\right)/3$ is the volume of the spherical cap.

(2) For $H > D/2$, the spherical cap becomes a full hemisphere of radius $\frac{D}{2}$ and polar angle $\frac{\pi}{2}$, i.e.,

$$R = \frac{D}{2}, \quad \varphi_{\max} = \frac{\pi}{2}. \qquad \textbf{[8]}$$

The deformed surface is composed of the hemisphere and a cylinder of height $h_c = H - D/2$ that is in contact with the vertical surface of the hole, as shown in Fig. S11*B*. Neglecting the friction between the PDMS and the vertical surface of the hole gives the uniform axial strain in the cylindrical part of PDMS, which also equals to the meridional strain in the hemisphere. Therefore the point separating the hemispherical and cylindrical parts has the radial coordinate

$$r_0 = \frac{\pi D^2}{2(\pi - 2)D + 8H} \qquad \textbf{[9]}$$

in the initial cylindrical coordinates ($r, \theta, 0$). The corresponding polar angle of the point is $\varphi = \frac{\pi r}{2r_0}$. The principle stretches for $r \le r_0$ are

$$\lambda_1^{\text{sphere}} = \frac{(\pi - 2)D + 4H}{2D}, \quad \lambda_2^{\text{sphere}} = \frac{D\sin\varphi}{2r}, \quad \lambda_3^{\text{sphere}} = \frac{4r}{\left[(\pi - 2)D + 4H\right]\sin\varphi}. \qquad \textbf{[10]}$$

The principle stretches for $r \ge r_0$ are

$$\lambda_1^{\text{contact}} = \frac{(\pi - 2)D + 4H}{2D}, \quad \lambda_2^{\text{contact}} = \frac{D}{2r}, \quad \lambda_3^{\text{contact}} = \frac{4r}{(\pi - 2)D + 4H}. \qquad \textbf{[11]}$$

The elastic strain energy is obtained as

$$U_e = 2\pi t \int_0^{r_0} \sum_{n=1}^{3} C_n \left(I_1^{\text{sphere}} - 3\right)^n r\mathrm{d}r + 2\pi t \int_{r_0}^{D/2} \sum_{n=1}^{3} C_n \left(I_1^{\text{contact}} - 3\right)^n r\mathrm{d}r. \qquad \textbf{[12]}$$

The work done by the pressure is

$$W = pV = \frac{1}{24}\pi D^2 (6H - D)p, \qquad [13]$$

where $V = \frac{1}{24}\pi D^2 (6H - D)$ is the volume enveloped by the deformed PDMS.

The principle of minimum potential energy gives

$$p = \frac{\partial U_e / \partial H}{\partial V / \partial H}. \qquad \textbf{[14]}$$

This gives analytically the relation between the pressure *p* and maximum deflection *H*.

Mechanics of the Tunable Photodetector Surface

As shown in Fig. S12, a flat PDMS membrane (of Young's modulus E and Poisson's ratio ν) with a square array of photodetectors on its top surface is installed on a water chamber. The open hole (of diameter D) at the top of the chamber confines the deformation of PDMS membrane during water extraction. The photodetector has a square shape of size l_{pd}=0.5 mm, and the spacing between adjacent photodetectors is l_{spacing}=0.42 mm. The area fraction of photodetectors is $f = l_{\text{pd}}^2 \big/ \left(l_{pd} + l_{spacing}\right)^2$. The position of each photodetector on the flat PDMS is expressed in cylindrical coordinates as (r, θ, $z=0$), as shown in Fig. S13*A*. The PDMS membrane deforms to a spherical cap of height H as water is extracted from the chamber (Fig. S13*B*). The radius of curvature is $R = \dfrac{D^2 + 4H^2}{8H}$, and polar angle $\varphi_{\max} = \sin^{-1} \dfrac{4DH}{D^2 + 4H^2}$ (Fig. S13*B*). The hemispherical profile can be expressed analytically in the cylindrical coordinates as $r^2 + \left(z - R + H\right)^2 = R^2$, or equivalently $r^2 + z^2 - \left(\dfrac{D^2}{4H} - H\right)z - \dfrac{D^2}{4} = 0$.

Finite element analysis (FEA) is also used to study the deformation of PDMS membrane and to track the positions of photodetectors during water extraction. Since its deformation is negligible, the water chamber is modeled as a rigid part and is fixed during the simulation. The PDMS membrane (thickness 0.5 mm, Young's modulus 2 MPa and Poisson's ratio 0.48) is clamped on the water chamber, and is modeled by continuum shell elements SC8R in the ABAQUS finite element program, since its thickness is much larger than photodetectors. Each photodetector is composed of polyimide (thickness 2.4 μm, Young's modulus 2.5 GPa and Poisson's ratio 0.34) and Si (thickness 1.2 μm, Young's modulus 130 GPa and Poisson's ratio 0.27), and is modeled by (composite) shell elements S4R, since it's very thin and has a multilayer structure. Uniform pressure is applied on the PDMS surface to simulate its deformation due to water extraction.

Figure S14*A* shows that the hemispherical profile $r^2 + z^2 - \left(\frac{D^2}{4H} - H\right)z - \frac{D^2}{4} = 0$ agrees very well with the experimentally measured profile and that obtained by FEM without any parameter fitting. This validates the analytical model, and confirms that the PDMS membrane indeed deforms into a hemispherical shape.

The hemispherical shape implies that the meridional strain in the PDMS membrane is uniform. Since the radius $D/2$ of the PDMS membrane on the open hole is stretched to the arc length $R\varphi_{\max}$, the photodetector initially at $(r, \theta, 0)$ in cylindrical coordinates has the spherical angle $\varphi = \frac{2r}{D}\varphi_{\max}$ on the hemisphere (Fig. S13*B*). The cylindrical coordinates of the photodetector after deformation are $\left(R\sin\varphi, \theta, R - H - R\cos\varphi\right)$, or equivalently,

$$\left[\frac{D^2+4H^2}{8H}\sin\left(\frac{2r}{D}\sin^{-1}\frac{4DH}{D^2+4H^2}\right), \theta, \frac{D^2-4H^2}{8H} - \frac{D^2+4H^2}{8H}\cos\left(\frac{2r}{D}\sin^{-1}\frac{4DH}{D^2+4H^2}\right)\right].$$

As shown in Figs. S14*B* and S14*C*, the above analytical expression for photodetector position agrees very well with the experiment and FEM without any parameter fitting. This provides further validation of the analytical model. The calculated circumferential and meridional strains in PDMS membrane are shown in Fig. S15*A* , S15*B*, respectively.

The deflection H can be obtained in terms of pressure p, using the same method as in the previous section. Linear elasticity is used due to small deformation of photodetector surface. Since silicon is several orders of magnitude more rigid than PDMS, the deformation of PDMS underneath photodetector is negligible. Therefore the circumferential strain and meridional strain are obtained as $\varepsilon_\varphi = \frac{2R\varphi_{\max} - D}{D\sqrt{1-f}}$ and $\varepsilon_\theta = \frac{R\sin\varphi - r}{r\sqrt{1-f}}$. The elastic strain energy is

$$U_{\mathrm{e}} = \frac{\pi t E}{1-\nu^2}\int_0^{D/2}\left(\varepsilon_\varphi^2 + \varepsilon_\theta^2 + 2\nu\varepsilon_\varphi\varepsilon_\theta\right)(1-f)r\mathrm{d}r. \qquad \textbf{[15]}$$

The work done by the pressure is given by Eqs. **7**. Then pressure p is given in terms of deflection H by Eqs. **14**, or equivalently $H=H(p)$.

Raytracing calculation and preliminary test of the tunable lens

Before the real imaging test with the tunable detector, the tunable lens is tested by both experiment and ray-tracing calculation. First, the tunable lens is qualitatively tested by viewing detector surface through the lens at several states of the lens deformations. As shown in the Fig. S16, field of view and magnification change according to deformation of lens surface. The properties of the lens are more quantitatively studied by ray tracing calculation. (Optical Bench)(16, 17) Rays originating from on an object plane, which is 67mm distant from the lens, pass through the lens and cross at points that define an imaging surface(13). By this method, the shape and the distance of detector surface can be determined at several states of lens deformation. (Fig. S17*A*) From this analysis, it is found out that the radius of curvature of lens surface is proportional to the distance and the radius of curvature of detector surface. (Fig. S17*B*, C) This prediction is validated by real testing at an optical bench. Fig. S18*A* shows setup for the real imaging experiment with the tunable lens and the tunable detector. Fig. S18*B*, *C*, *D*, *E* show formed image on a flat diffusive screen at four different states of the lens deformation. These images are taken by a commercial digital camera at the back side of diffusive screen. (EOS-1Ds Mark III, Canon) Dashed lines in red are showing the actual size of the tunable detector. These flat screen images are off-focused at the periphery, which is obvious at the lowest magnification. (Fig. S18*B*)

Imaging Result

To demonstrate the operation of the tunable hemispherical imaging system, two types of imaging experiment are performed. One experiment shows focusing effects. In this experiment, a plano-convex lens (diameter of 9 mm and focal length of 22.8 mm, JML Optical Industries, Inc) is used. Fig. S19 show series of images at different deformation of detector surface placing in front of exact focal distance. As deformation of the detector become larger, the distance approaches the ideal focal distance, and images come into focus.
Another experiment involves the tunable lens in the imaging. As already known from the preliminary study of the tunable lens, the focal distance and the radius of curvature of the detector surface depend on the geometry of the lens. At each state of lens deformation, the

detector surface is deformed to match with the radius of curvature from ray-tracing calculation. As a result, acquired images at this setup show uniform focus and intensity distribution. (Fig. S20*A*, *B*, *C*, *D*) For comparison, acquired images in the flat state are shown. (Fig. S20*E*, *F*, *G*, *H*) The clearest differences between the images from curved surface and flat surface can be found at the lowest magnification images. (Fig. S20*A*, *E*) This advantage of curved screens over flat screens agrees with the previously reported result (1, 13). Fig. S21 shown I-logo imaged at two different magnification states. The right image shows three times higher optical magnification than the left image.

References

1. Ko HC, et al. (2008) A hemispherical electronic eye camera based on compressible silicon optoelectronics. *Nature* 454: 748-753.

2. Meitl MA, et al. (2006) Transfer printing by kinetic control of adhesion to an elastomeric stamp. *Nature Materials* 5: 33-38.

3. Kim DH, et al. (2009) Ultrathin silicon circuits With strain-isolation layers and mesh layouts for high-performance electronics on fabric, vinyl, leather, and paper. *Adv Mater* 21: 3703-3707.

4. Tsai FS, et al. (2008) Miniaturized universal imaging device using fluidic lens. *Opt Lett* 33: 291-293.

5. Tsai FS, et al. (2010) Fluidic lens laparoscopic zoom camera for minimally invasive surgery. *J Biomed Opt* 15: 030504-1-030504-3.

6. Yu HB, Zhou GY, Leung HM, Chau FS (2010)Tunable liquid-filled lens integrated with aspherical surface for spherical aberration compensation. *Opt Express* 18: 9945-9954.

7. Zhang DY, et al. (2003) Fluidic adaptive lens with high focal length tunability. *Appl Phys Lett* 82: 3171-3172.

8. Dong L, Agarwal AK, Beebe DJ, Jiang HR (2006) Adaptive liquid microlenses activated by stimuliresponsive hydrogels *Nature* 442: 551-554.

9. Dong L, Agarwal AK, Beebe DJ, Jiang HR (2007) Variable-focus liquid microlenses and microlens arrays actuated by thermoresponsive hydrogels. *Adv Mater* 19: 401-406.

10. Tang SKY, Stan CA, Whitesides GM (2008) Dynamically reconfigurable liquid-core liquid-cladding lens in a microfluidic channel. *Lab Chip* 8: 395-401.

11. Zhu DF, Li CH, Zeng XF, Jiang HR (2010) Tunable-focus microlens arrays on curved surfaces. *Appl Phys Lett* 96: 081111-1-081111-3.

12. Shin G, et al. (2010) Micromechanics and advanced designs for curved photodetector arrays in hemispherical electronic-eye cameras. *Small* 6: 851-856.

13. Jung I, et al. (2010) Paraboloid electronic eye cameras using deformable arrays of photodetectors in hexagonal mesh layouts. *Appl Phys Lett* 96: 021110-1- 021110-3.

14. Schneider F, Fellner T, Wilde J, Wallrabe U (2008) Mechanical properties of silicones for MEMS. *J Micromech Microeng* 18: 065008.

15. Yeoh OH (1993) Some forms of the strain energy function for rubber. *Rubber Chem Technol* 66: 754-771.

16. Born M, Wolf E (1999) *Principles of Optics* (Cambridge Univ. Press, New York).

17. Walther A (1995) *The Ray and Wave Theory of Lenses* (Cambridge Univ. Press, Cambridge, UK).

Supplementary Figures and Legends

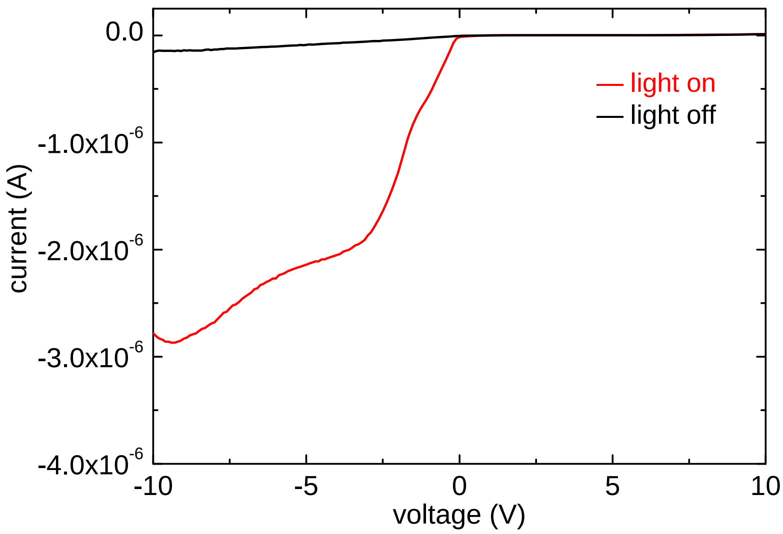

Fig. S1. Representative current-voltage response of a pixel at the center of the array, with a light source on (red) and off (black).

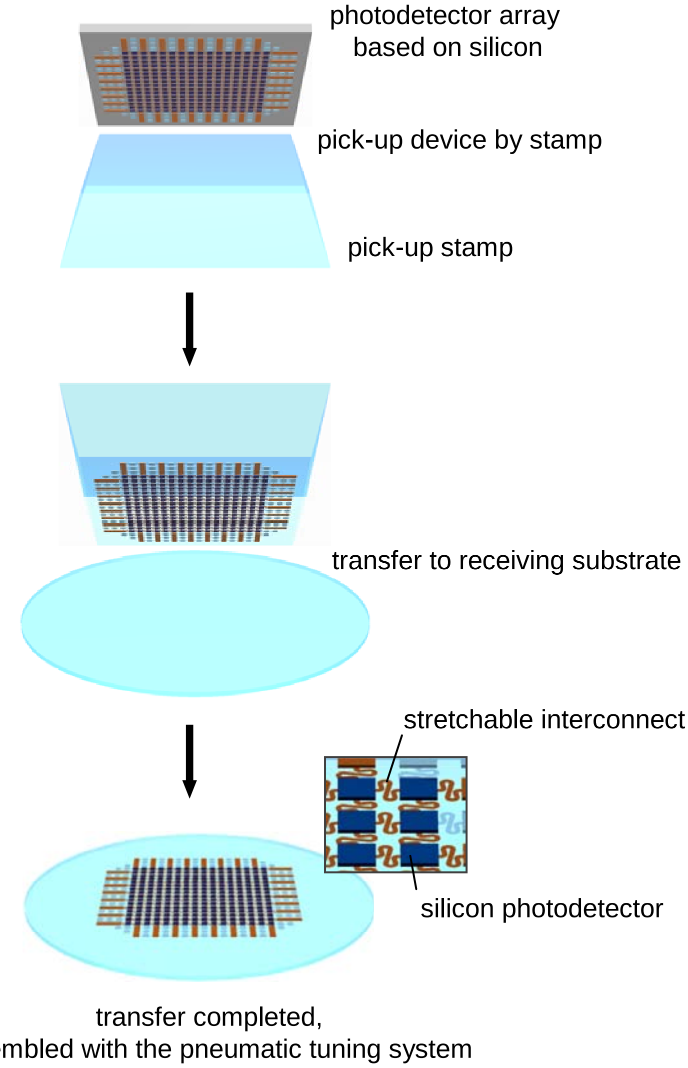

Fig. S2. Schematic illustration of steps for transferring photodetectors array onto PDMS membrane substrate.

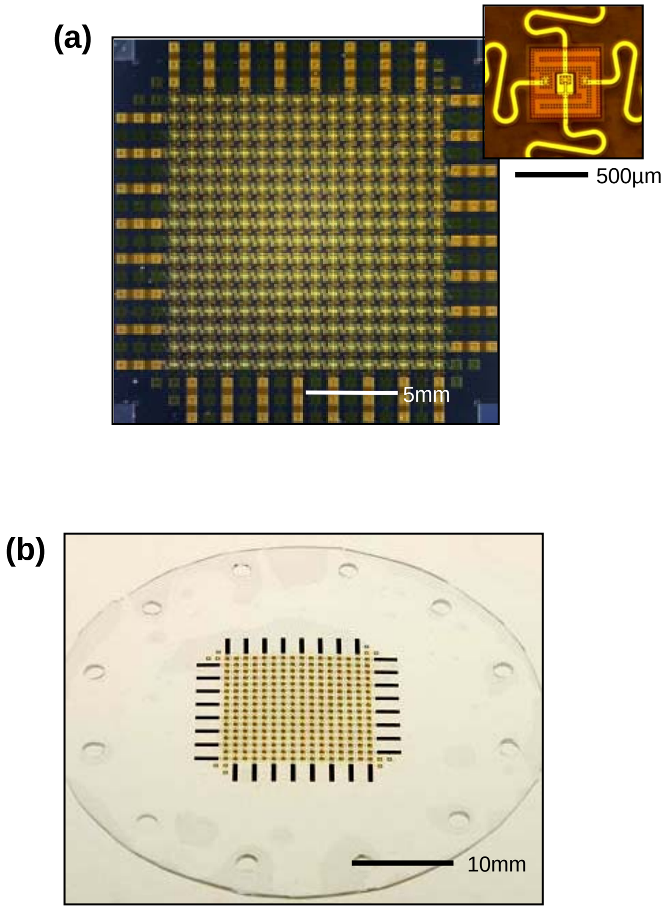

Fig. S3. (a) Photograph of a photodetector/diode array before transfer on a planar surface. Optical microscope image of single photodetector (inset). (b) Transferred photodetector array on PDMS membrane substrate.

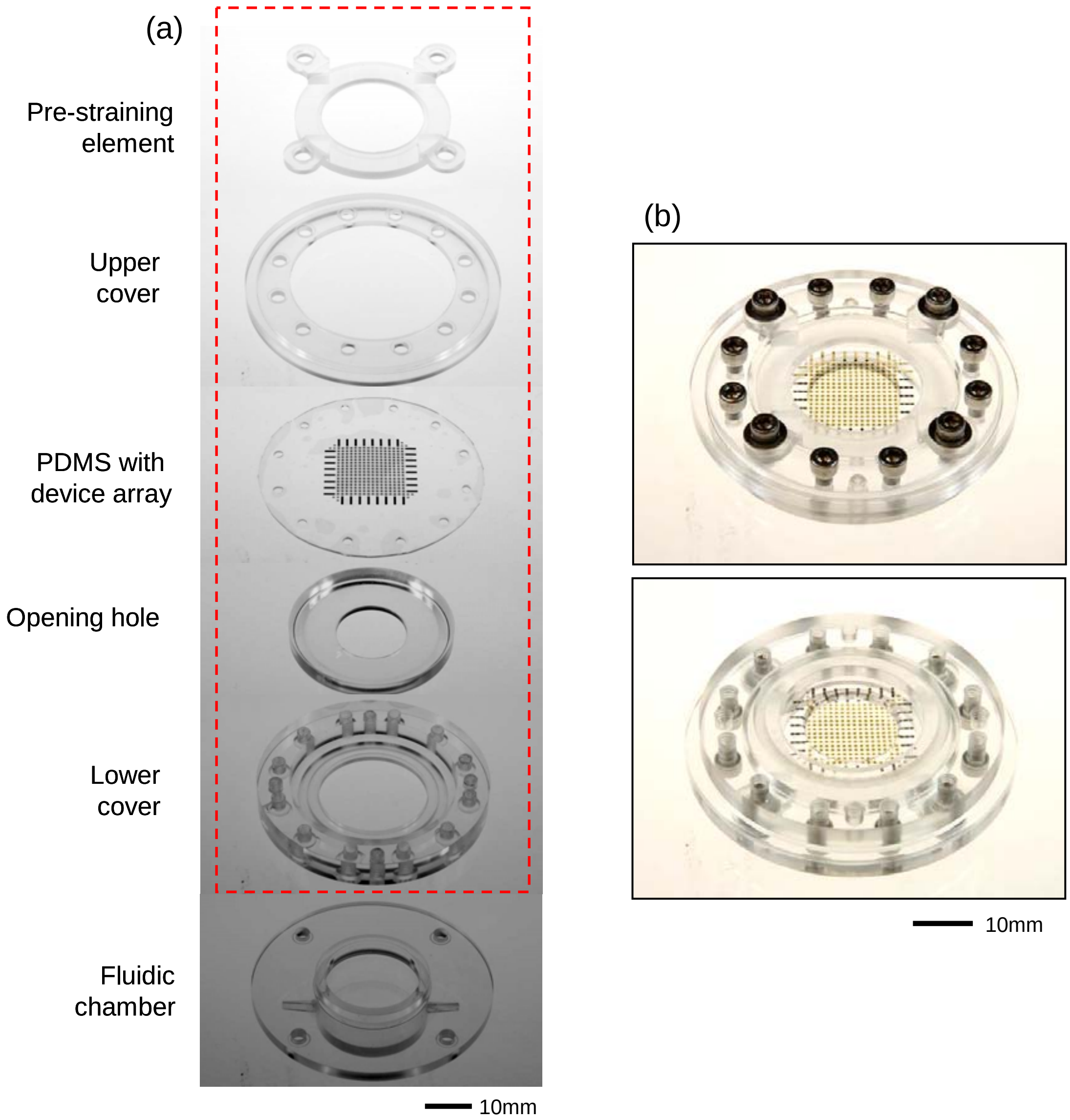

Fig. S4. (a) Photograph of elements for completing the fluidic deformation system. (b) Top down view of the cover assembly for the fluidic deformation system, which is composed of components in the dashed rectangle in the left figure (upper), bottom up view of the cover assembly (lower).

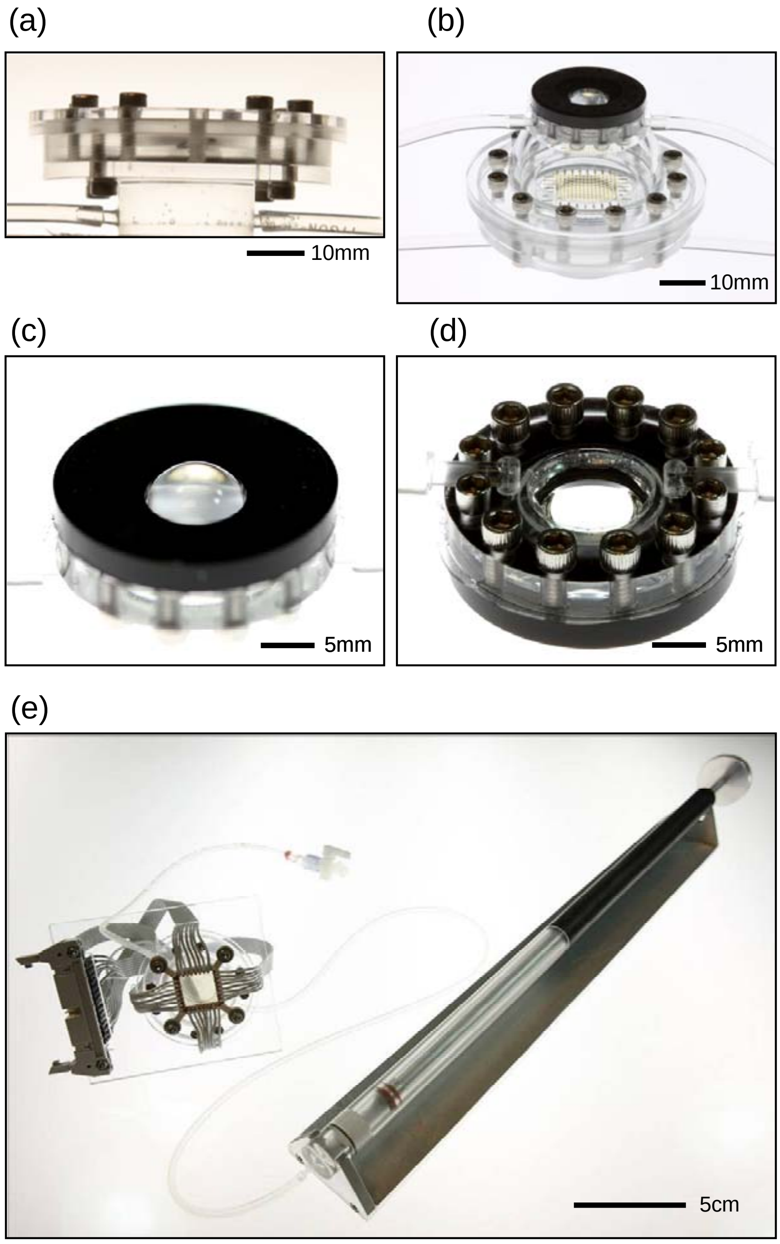

Fig. S5. (a) The side view of the tunable detector which connected with in/out tubes. (b) Photograph a built system with the tunable lens placing above the tunable detector. (c) The top-down view of the tunable lens. (d) The bottom-up view of the tunable lens. (e) The completed camera connected to a custom made syringe.

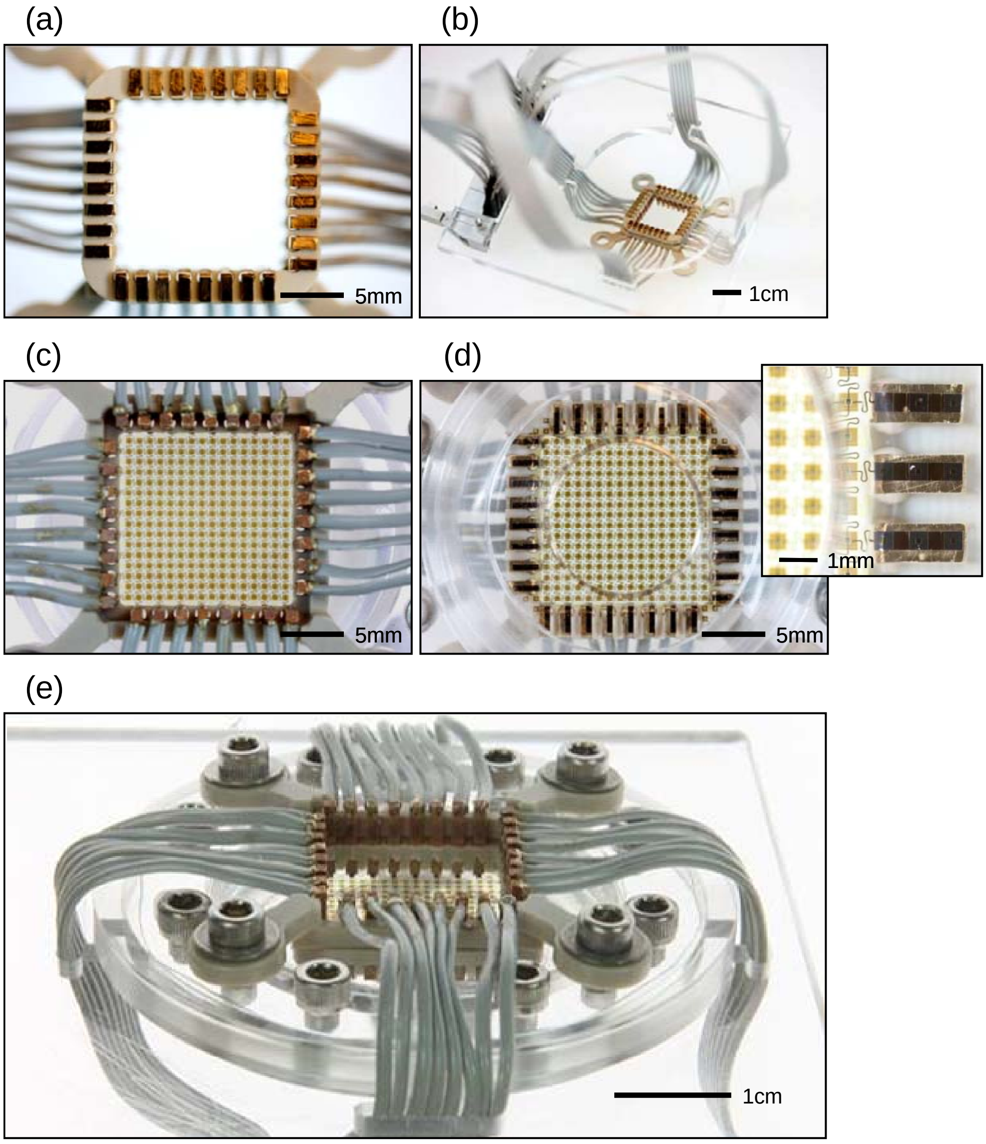

Fig. S6. (a) Photograph of contacting electrodes pin assembly before surface polishing and metal layer deposition (b) Photograph of the mounting board with electrodes pin array assembled (c) The top down photograph of electrodes pin array installed on a photodetector/diode array (d) The bottom up view of electrodes pin array installed on a photodetector/diode array, close-up view of the area where electrode pins are pressing electrodes of device array (inset). (e) A tilted view of the pressing bar element which has four cantilever springs at the corner.

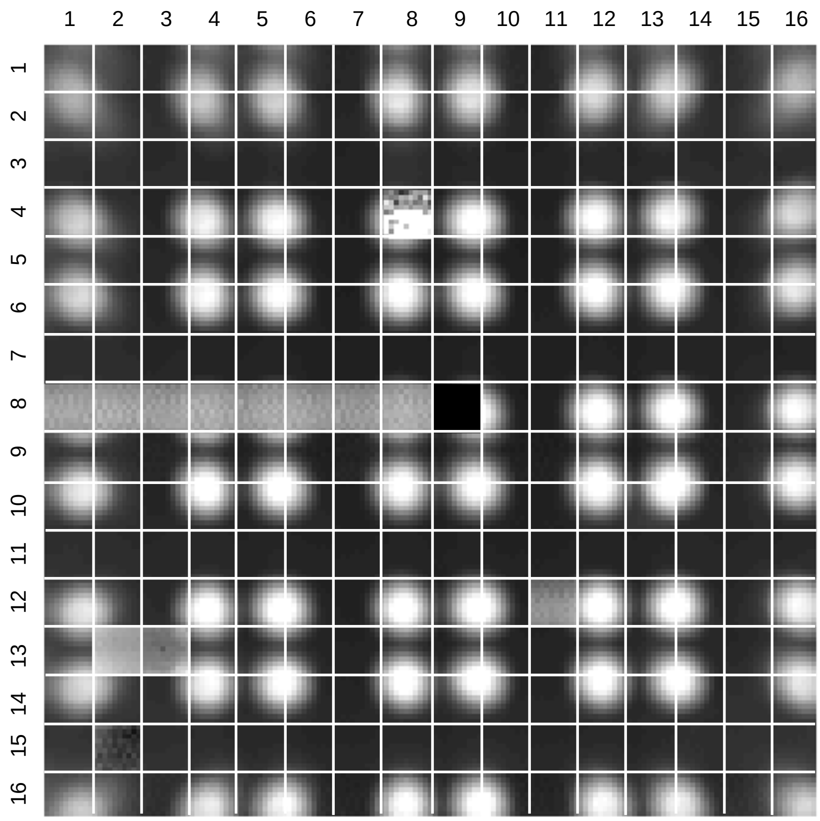

Fig. S7. Device yield of working camera used in the imaging experiments. In this experiment, a plano-convex lens (diameter of 9 mm and focal length of 22.8 mm, JML Optical Industries, Inc) is used.

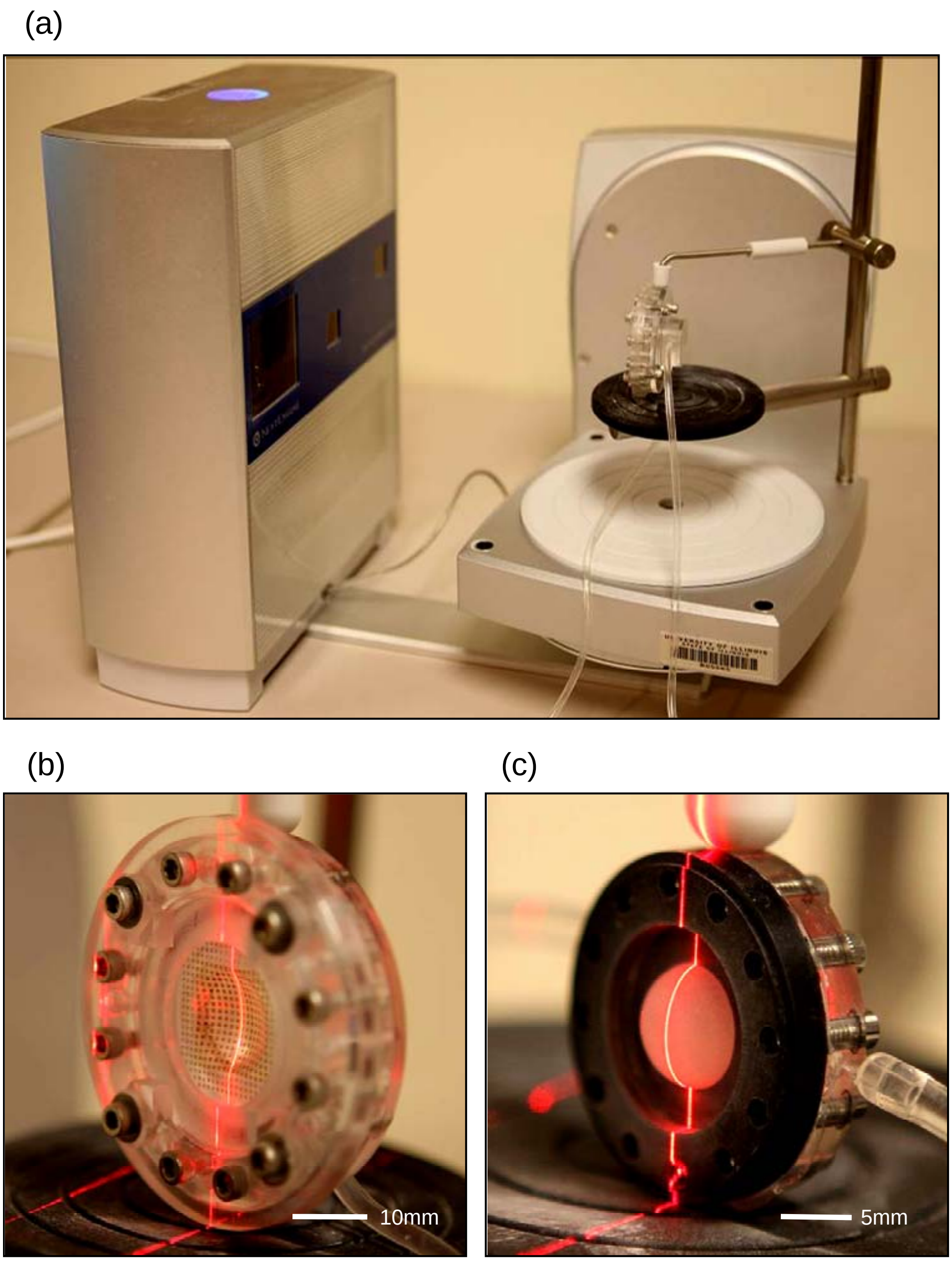

Fig. S8. (a) The 3D laser scanning system for measuring surface profile. (b) The tunable detector is being scanned. (c) The tunable lens is being scanned.

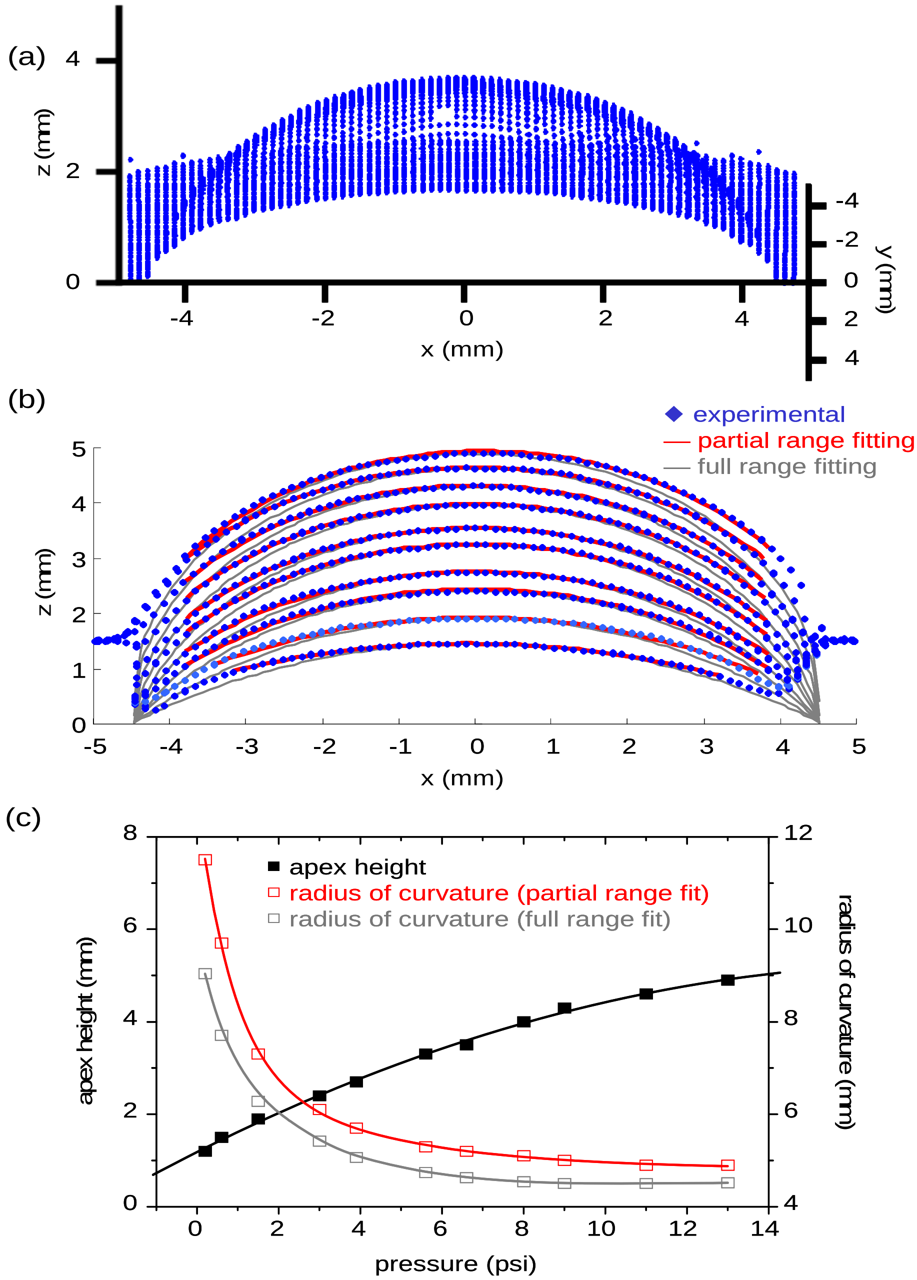

Fig. S9. (a) Raw point data of deformed lens surface acquired by 3D scanner. (b) Measured profiles and fitted curves of lens surface at various states of deformation. (c) The apex height and the radius of curvature along the pressure change.

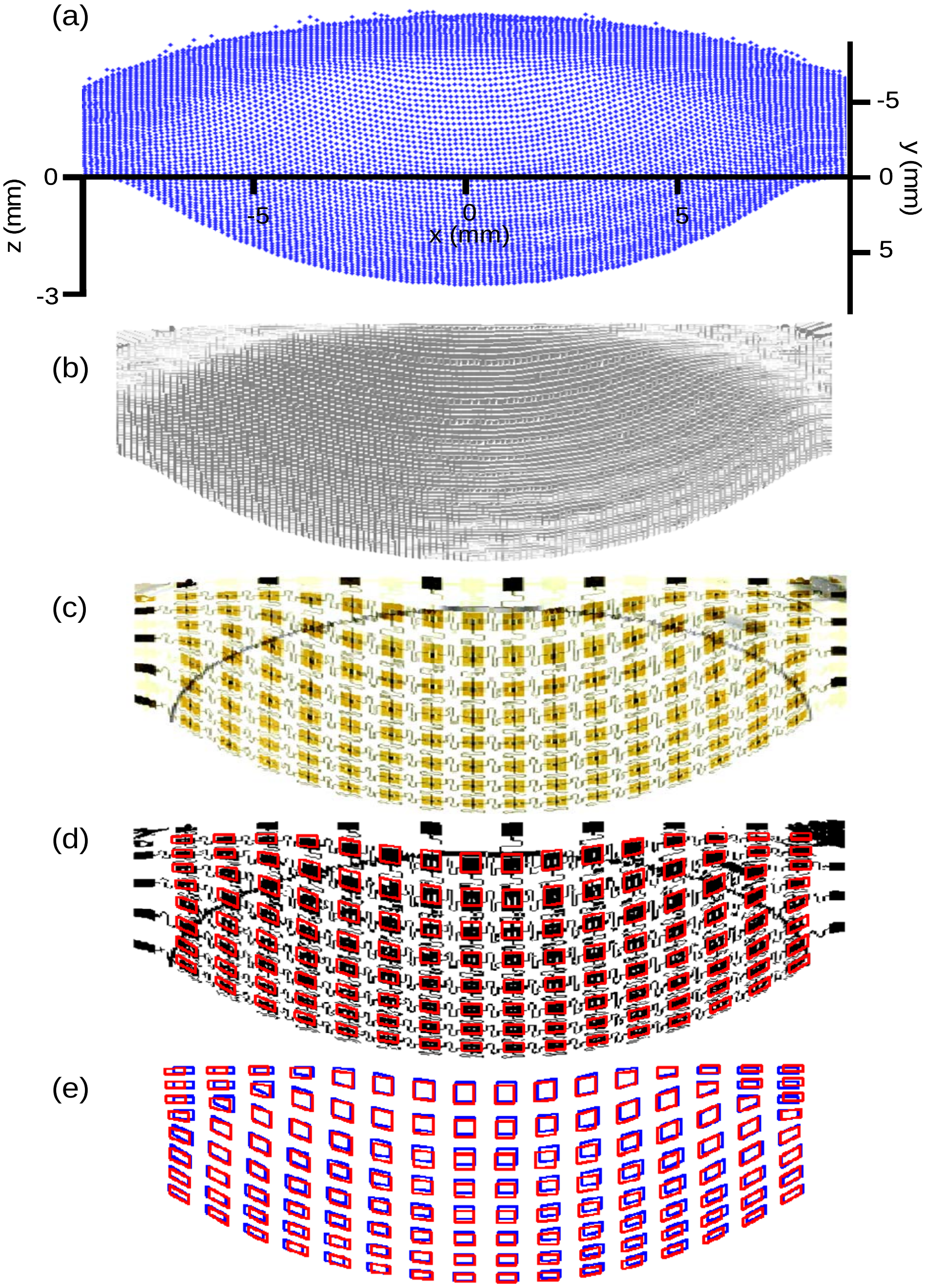

Fig. S10. Measurement scheme of pixel position: (a) Raw point data of deformed detector surface acquired by 3D scanner. (b) Generated surface by raw data. (c) Top-down view of device array projected on the generated surface. (d) Measured pixel position (red square) is overlapped on the detector surface. (e) Analytically calculated position (blue square) is overlapped on measured position (red square).

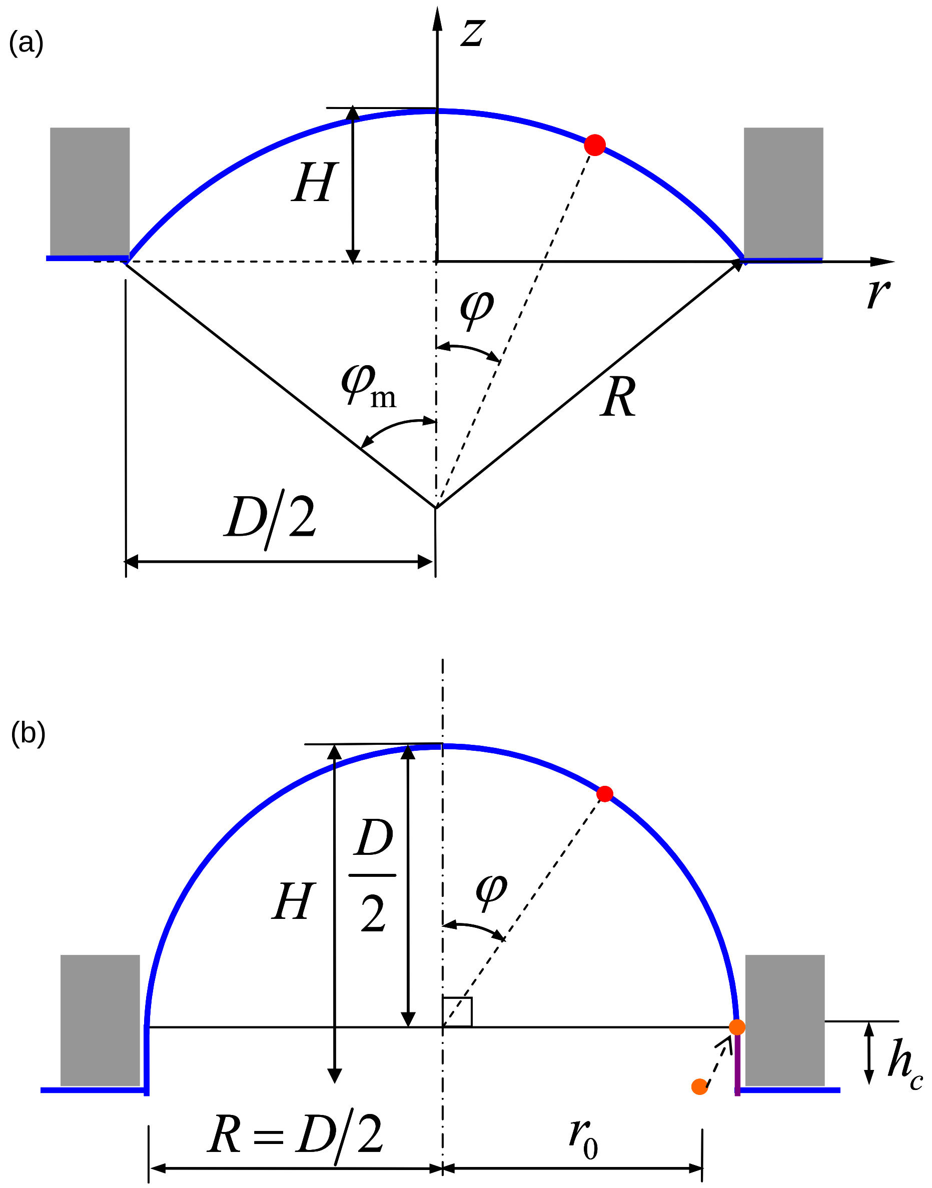

Fig. S11. (a) The lens deforms to be a spherical cap for deflection $H \leq D/2$. (b) For deflection $H > D/2$, the lens surface has contact with the sidewall of the top plate. Its deformed shape consists of a full hemisphere and a short cylinder.

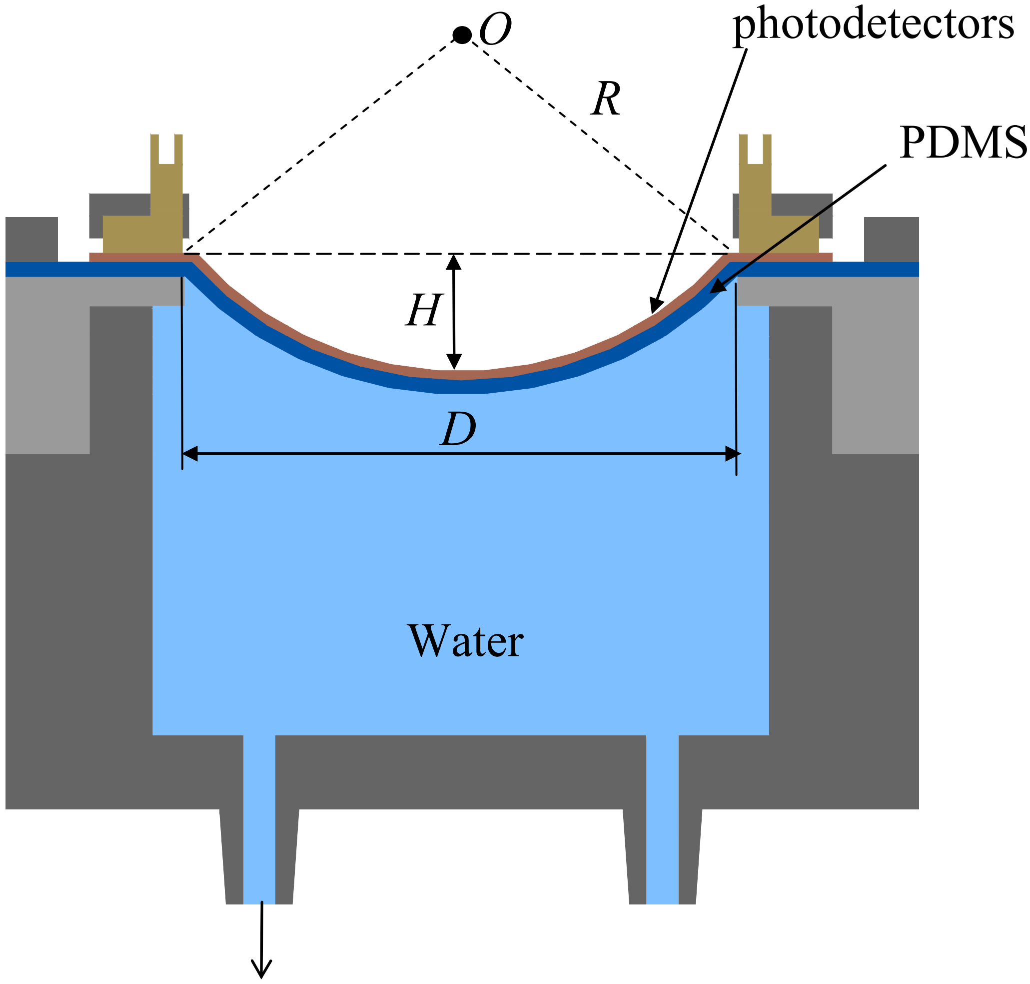

Fig. S12. (a) Schematic illustration of the deformation of photodetector surface due to water extraction.

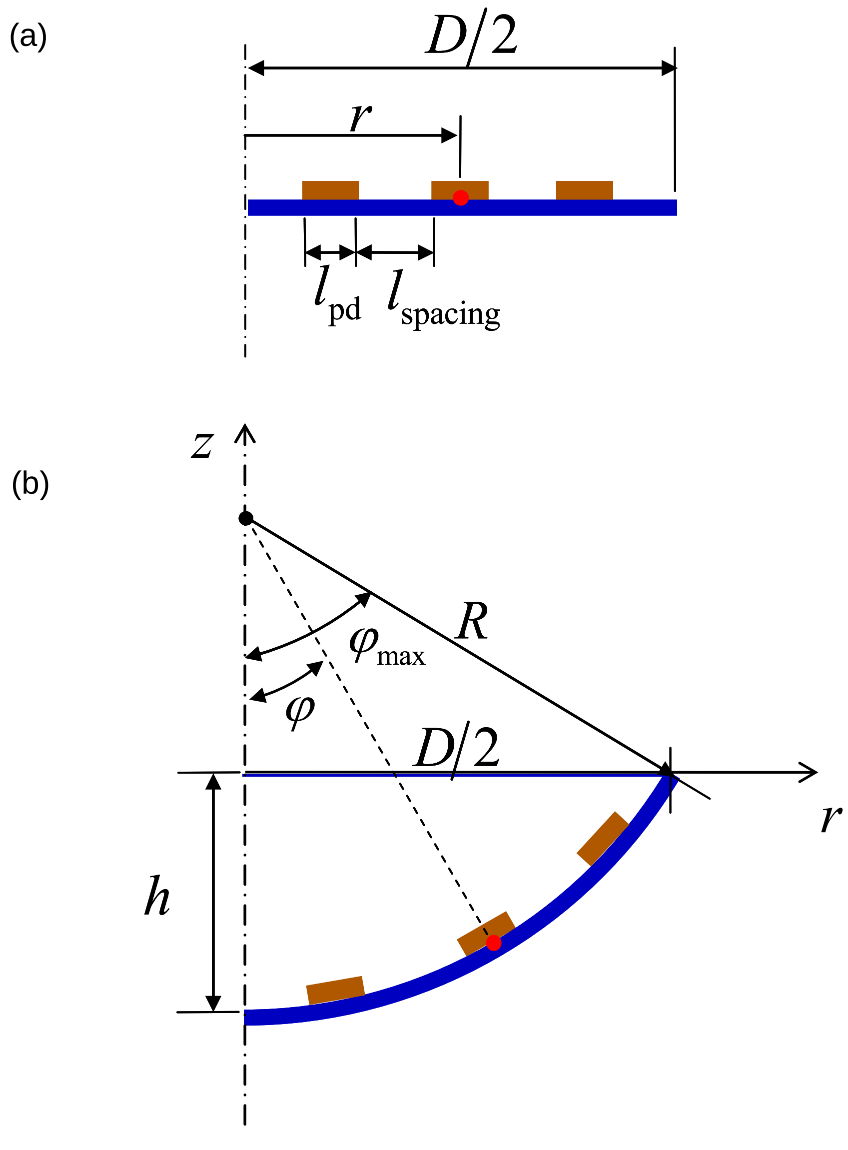

Fig. S13. (a) Schematic illustration of photodetectors on undeformed PDMS surface. (b) Schematic illustration of photodetectors on deformed PDMS surface.

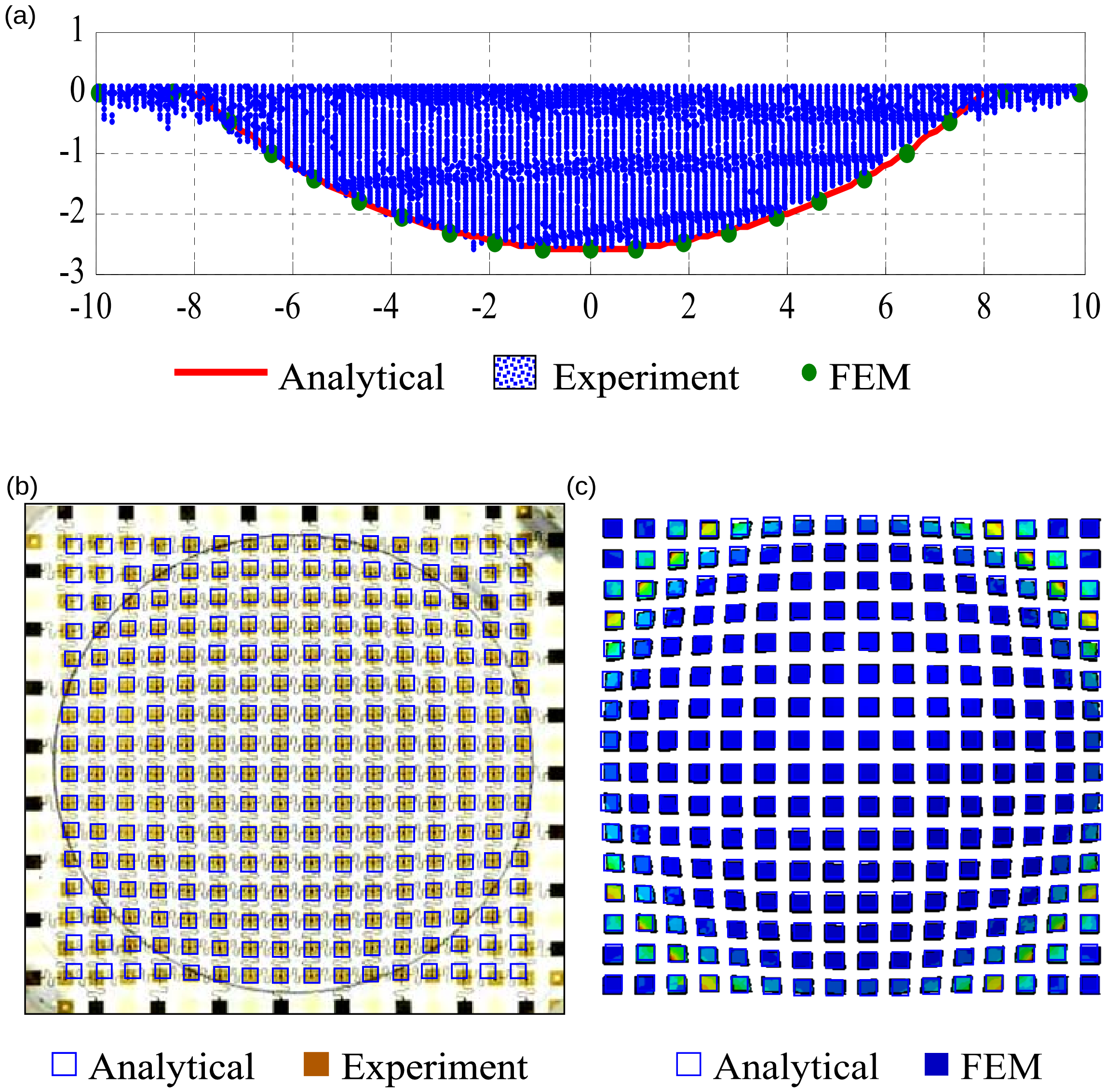

Fig. S14. (a) The shape of deformed photodetector surface given by analytical solution shows good agreement with experiment and finite element analysis for 2.69 mm deflection. The analytically given photodetector positions shows good agreement with experiment (b) and finite element analysis (c).

(a)

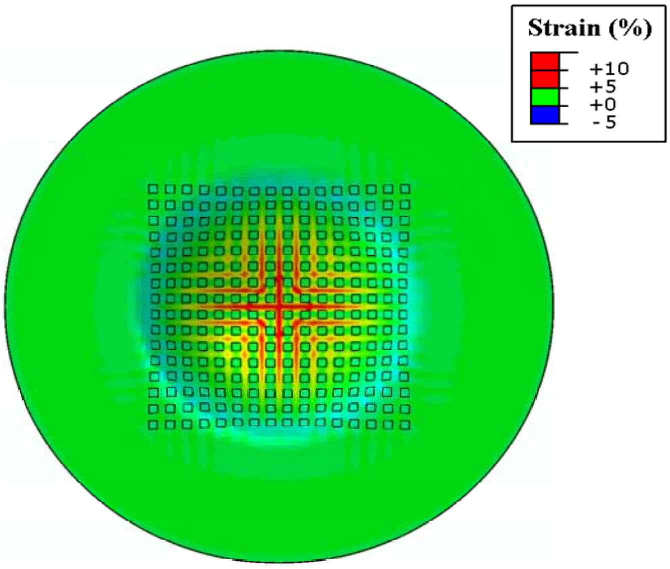

(b)

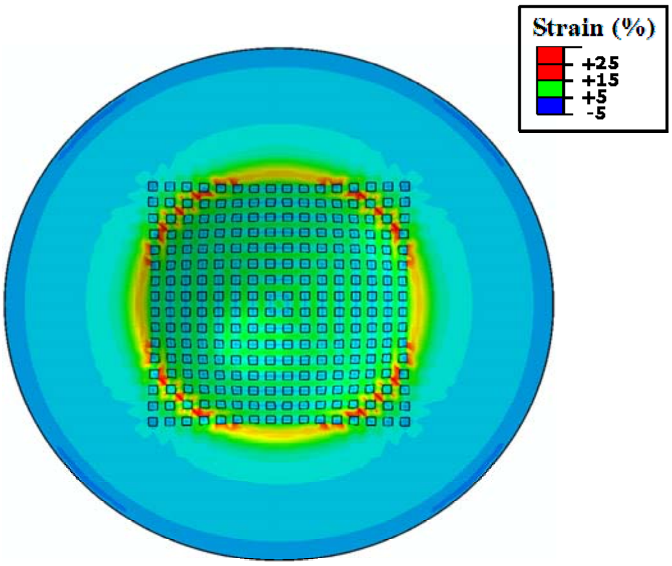

Fig. S15. (a) Circumferential strain in PDMS membrane (b) Meridional strain in PDMS membrane.

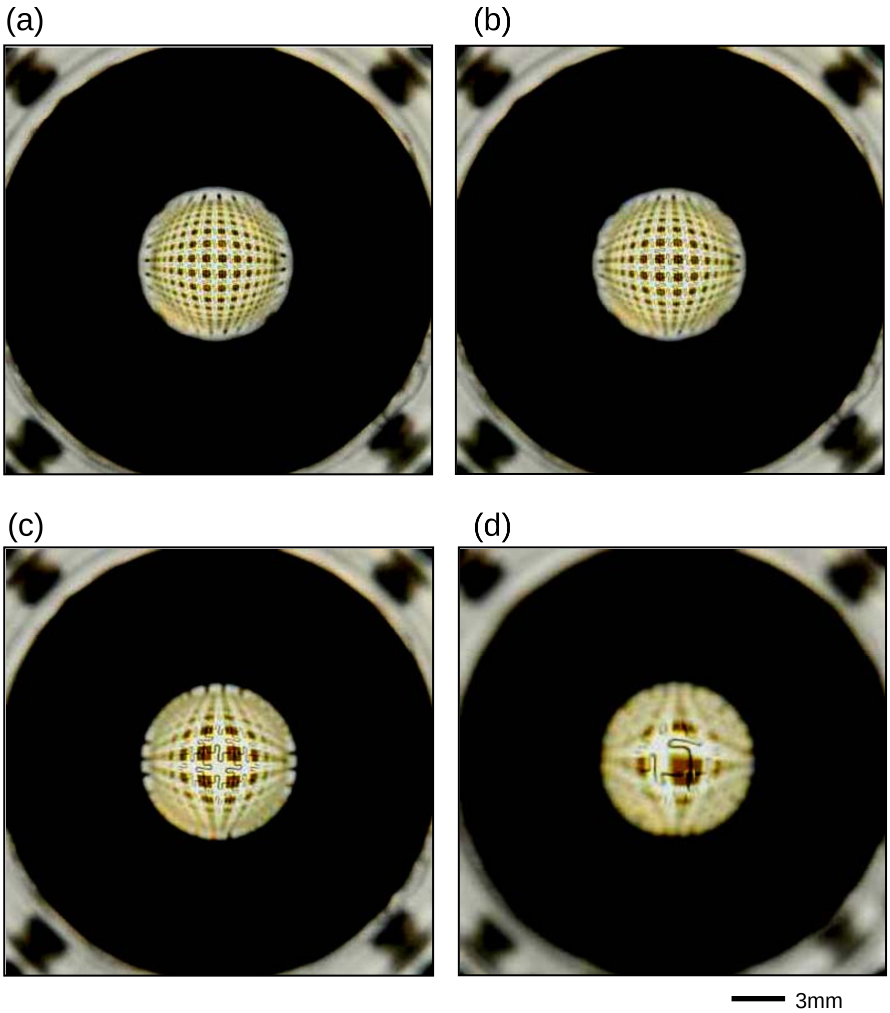

Fig. S16. Photographs of the tunable detector imaged through the tunable lens at four different lens geometries: (a) radius of curvature of lens surface R_L=4.9mm, (b) R_L=6.1mm, (c) R_L=7.3mm, (d) R_L=11.5mm. (The distance from the bottom of the lens to the bottom of the detector is z=25.0mm for all cases.)

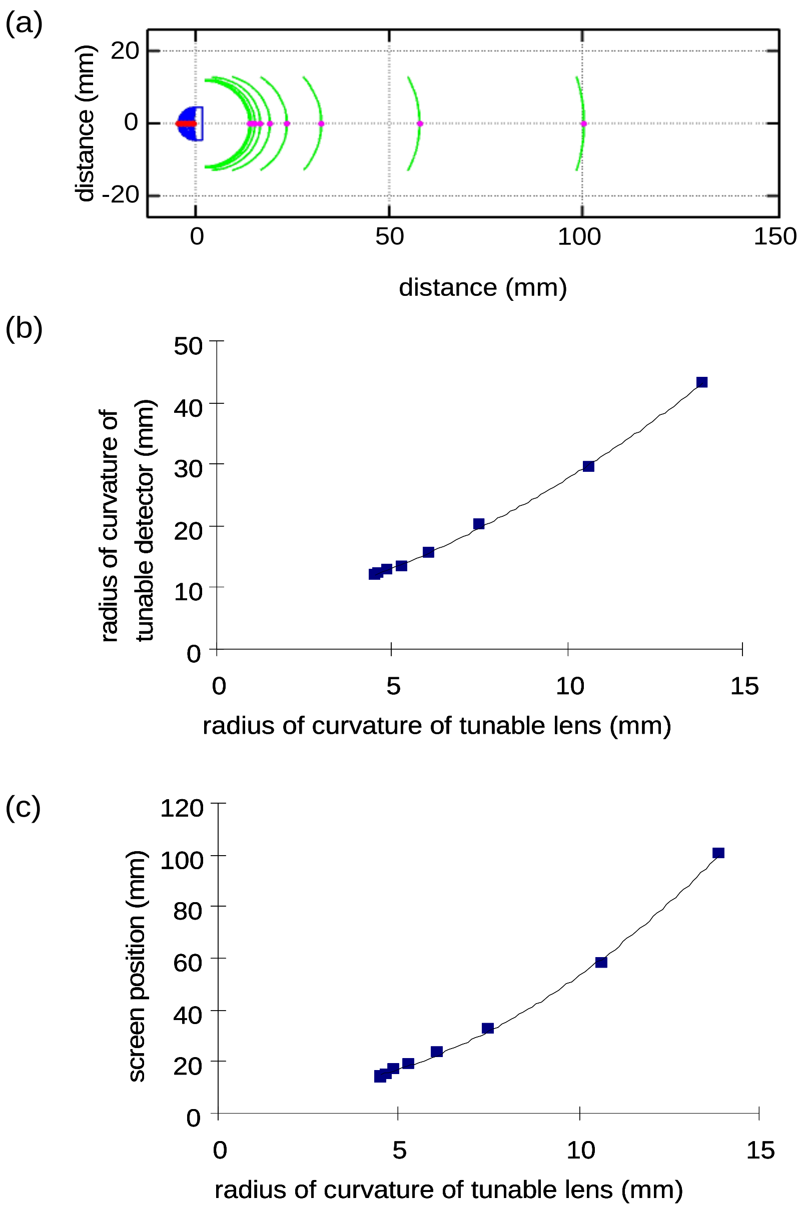

Fig. S17. (a) The shapes of lens surfaces and corresponding shapes and distances detector surfaces by raytracing calculation, (b) Relation between radius of curvature of lens and radius of curvature of detector, (c) Relation between radius of curvature of lens and distances from lens.

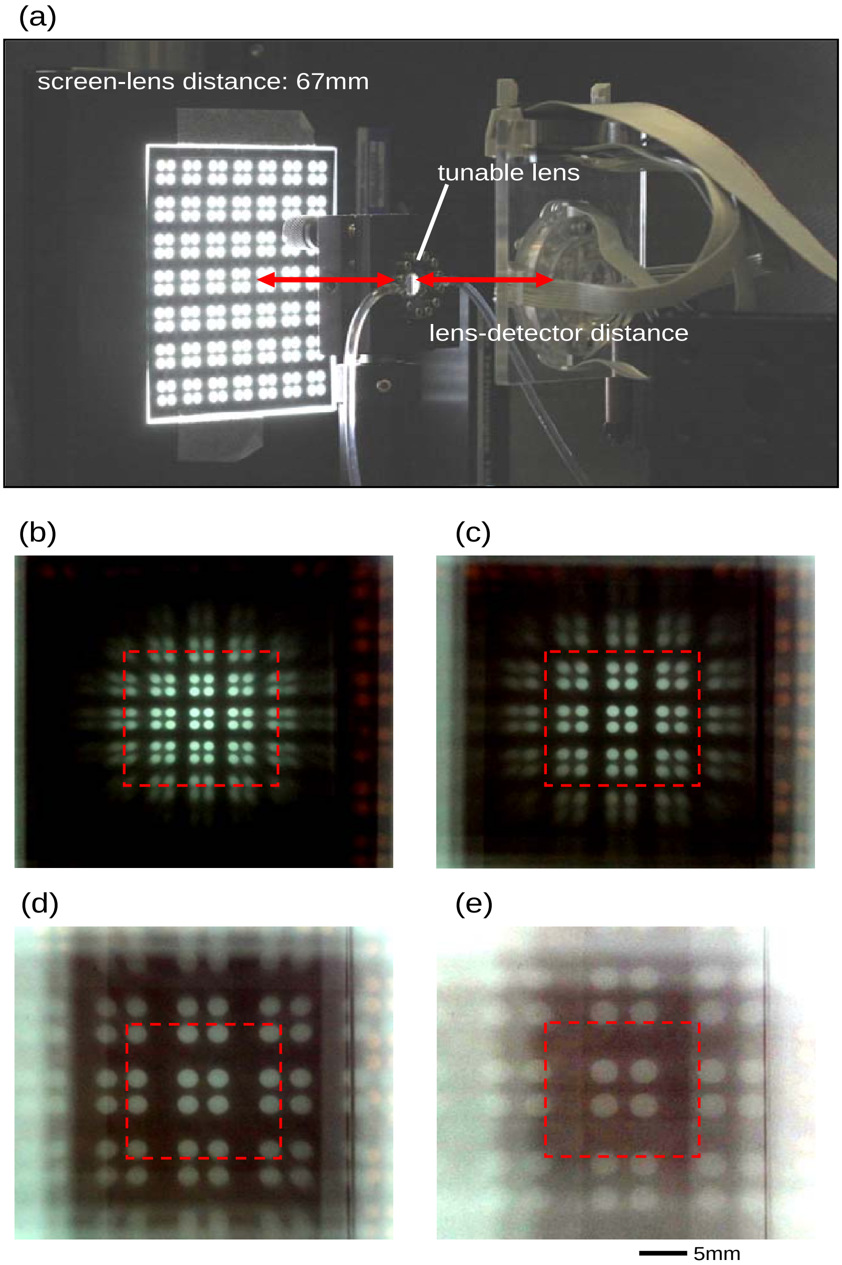

Fig. S18. (a) Photograph of the optical setup for image acquisition. Photographs of image formed by tunable lens at a flat diffusive screen: (b) distance from the lens z=16mm, radius of curvature of lens surface R_L=4.9mm, (c) z=24mm, R_L=6.1mm, (d) z=38mm, R_L=7.3mm, (e) z=55mm, R_L=11.5mm.

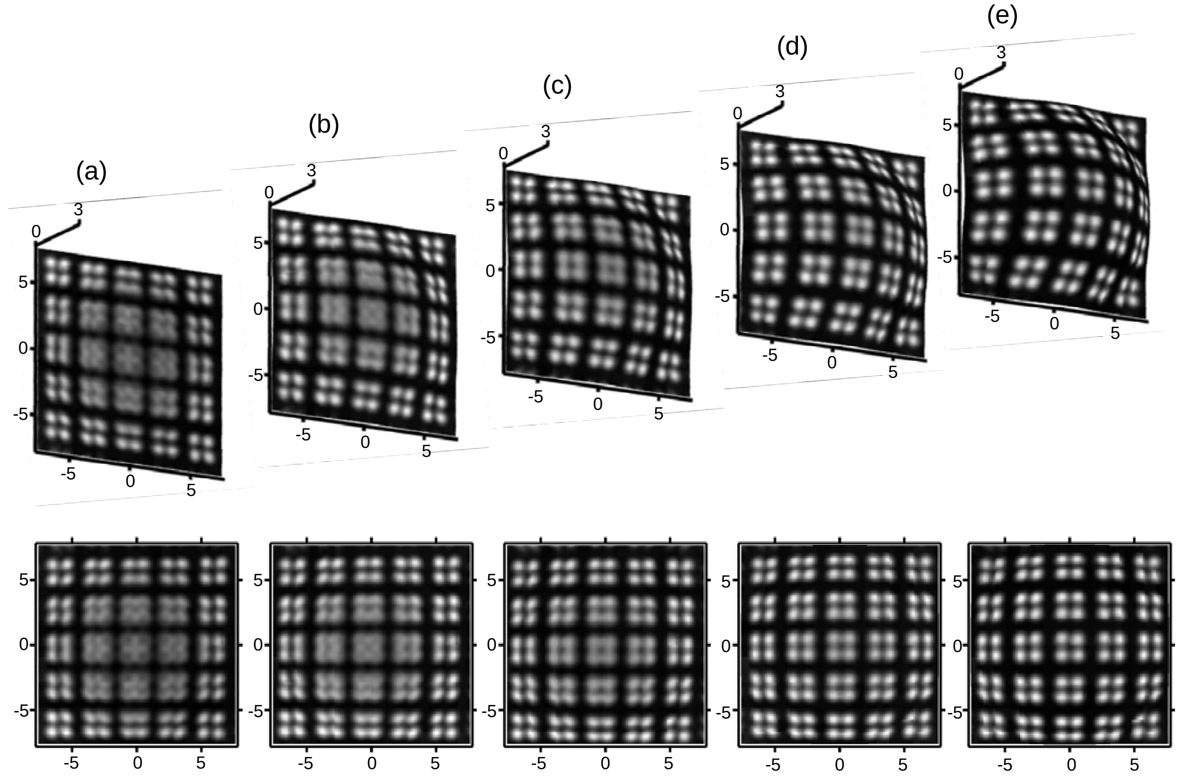

Fig. S19. Images acquired by the tunable detector at different deformations of detector surfaces: (a) flat detector surface, (b) the radius of curvature R_D=88.7mm and the bottom depth H_D= 0.4 mm, (c) R_D=42.0mm, H_D= 0.8 mm, (d) R_D=24.1mm, H_D= 1.4 mm, (e) R_D=16.2mm, H_D= 2.2 mm.

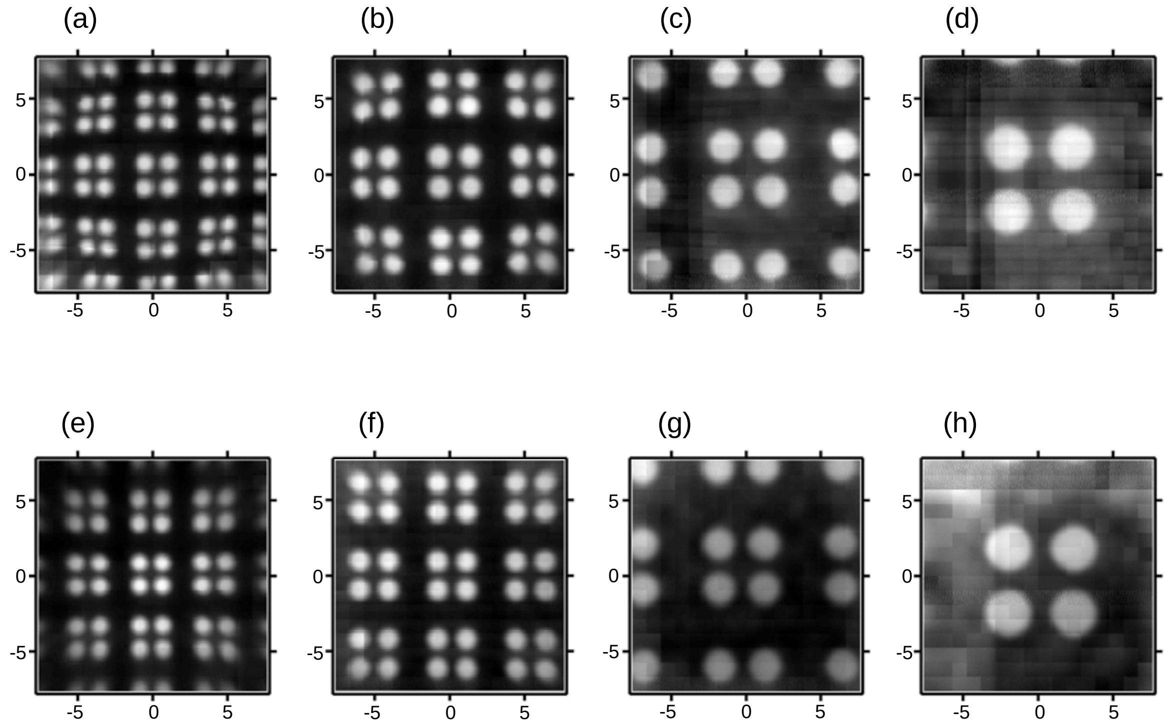

Fig. S20. Images acquired by the tunable detector and the tunable lens at four imaging conditions: (a) distance from the lens z=16mm, radius of curvature of lens surface R_L=4.9mm, radius of curvature of detector surface R_D=11.4mm, (b) z=24mm, R_L=6.1mm, R_D=14.0mm, (c) z=38mm, R_L=7.3mm, R_D=19.2mm, ,(d) z=52mm, R_L=11.5mm, R_D=25.7mm, (e) flat detector surface at the condition (a), (f) flat detector surface at the condition (b), (g) flat detector surface at the condition (c), (h) flat detector surface at the condition (d).

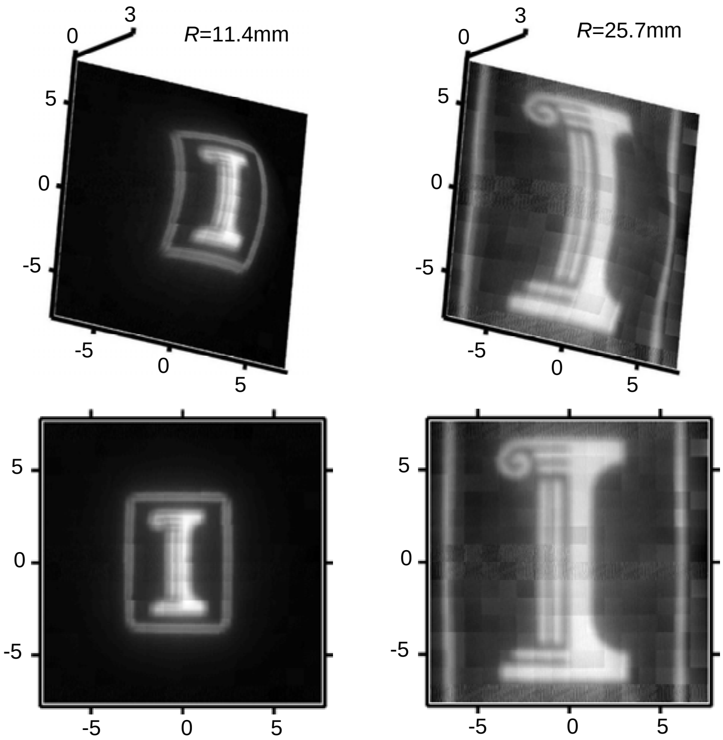

Fig. S21. Images of the University of Illinois 'I' logo acquired by the tunable detector and the tunable lens at different imaging conditions. The left- and right-hand images are taken at distances from the lens z=16mm, 48mm and radius of curvatures of lens surfaces R_L=4.9mm, 9.7mm and radius of curvatures of the detector surfaces R_D=11.4mm, 25.7mm (from left to right). Projected views of the each image are shown below. The distance between the lens and source image is 67mm. The axis scales are in millimeters.

Supporting Information

Jung et al. 10.1073/pnas.1015440108

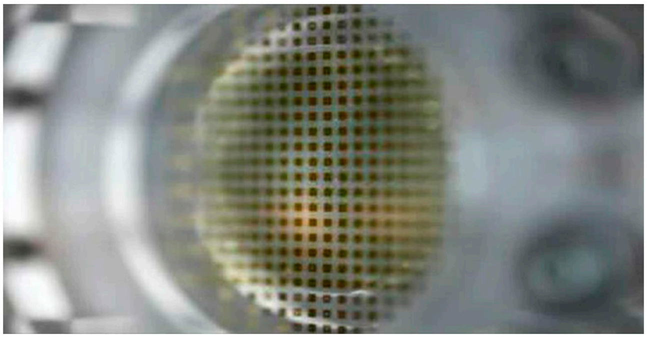

Movie S1. Real-time movie about deformation of detector surface.

Movie S1 (MPG)